


Structural Basis of the Oncogenic Interaction of Phosphatase PRL-1 with the Magnesium Transporter CNNM2*[‡]♦

Received for publication, September 23, 2016, and in revised form, November 28, 2016 Published, JBC Papers in Press, November 29, 2016, DOI 10.1074/jbc.M116.759944

Paula Giménez-Mascarell,^{a1} Iker Oyenarte,^{a1} Serge Hardy,^{b2} Tilman Breiderhoff,^{c,d3} Marchel Stuver,^e Elie Kostantin,^{b,f} Tammo Diercks,^a Angel L. Pey,^{g4} June Ereño-Orbea,^a María Luz Martínez-Chantar,^h Reham Khalaf-Nazzal,ⁱ Felix Claverie-Martin,^{j5} Dominik Müller,^{c3,6} Michel L. Tremblay,^{b,f,k2,7} and  Luis Alfonso Martínez-Cruz^{a8}

From the ^aStructural Biology Unit, Center for Cooperative Research in Biosciences (CIC bioGUNE), Technology Park of Bizkaia, 48160 Derio, Bizkaia, Spain, the ^bRosalind and Morris Goodman Cancer Research Centre, ^cDepartment of Biochemistry, and ^kDivision of Experimental Medicine, Department of Medicine, McGill University, Montreal, Quebec H3A 1A3, Canada, the ^dDepartment of Pediatric Nephrology, Charité Universitäts Medizin, Berlin, 13353 Berlin, Germany, the ^eBerlin Institute of Health, Berlin, Germany, the ^fIn-Cell NMR Laboratory, Department of NMR-supported Structural Biology, Leibniz Institute of Molecular Pharmacology (FMP Berlin), Robert-Rössle Strasse 10, 13125 Berlin, Germany, the ^gDepartment of Physical Chemistry, Faculty of Sciences, University of Granada, Av. Fuentenueva s/n, 18071 Granada, Spain, the ^hMetabolomics Unit, Center for Cooperative Research in Biosciences (CIC bioGUNE), Technology Park of Bizkaia, 48160 Derio, Bizkaia, Spain, the ⁱDepartment of Biomedical Sciences, An-Najah National University, P. O. Box 7, Nablus, Palestinian Territory, and the ^jResearch Unit, Nuestra Señora de Candelaria University Hospital, 38010 Santa Cruz de Tenerife, Spain

Edited by Roger J. Colbran

Phosphatases of regenerating liver (PRLs), the most oncogenic of all protein-tyrosine phosphatases (PTPs), play a critical role in metastatic progression of cancers. Recent findings established a new paradigm by uncovering that their association with magnesium transporters of the cyclin M (CNNM) family causes a rise in intracellular magnesium levels that promote oncogenic transformation. Recently, however, essential roles for regulation of the circadian rhythm and reproduction of the CNNM family have been highlighted. Here, we describe the crystal structure of PRL-1 in complex with the Bateman module of

CNNM2 (CNNM2_{BAT}), which consists of two cystathionine β -synthase (CBS) domains (IPR000664) and represents an intracellular regulatory module of the transporter. The structure reveals a heterotetrameric association, consisting of a disc-like homodimer of CNNM2_{BAT} bound to two independent PRL-1 molecules, each one located at opposite tips of the disc. The structure highlights the key role played by Asp-558 at the extended loop of the CBS2 motif of CNNM2 in maintaining the association between the two proteins and proves that the interaction between CNNM2 and PRL-1 occurs via the catalytic domain of the phosphatase. Our data shed new light on the structural basis underlying the interaction between PRL phosphatases and CNNM transporters and provides a hypothesis about the molecular mechanism by which PRL-1, upon binding to CNNM2, might increase the intracellular concentration of Mg²⁺ thereby contributing to tumor progression and metastasis. The availability of this structure sets the basis for the rational design of compounds modulating PRL-1 and CNNM2 activities.

* This work was supported in part by Departamento de Educación, Universidades e Investigación del Gobierno Vasco Grant PI2010-17, Departamento de Industria, Innovación, Comercio y Turismo del Gobierno Vasco Grants ETORTEK IE05-14 and IE07-202], Diputación Foral de Bizkaia Grants 7/13/08/2006/11 and 7/13/08/2005/14, Spanish Ministerio de Ciencia e Innovación (MICINN) Grant BFU2010-17857, Spanish Ministry of Economy and Competitiveness Grant BFU2013-47531-R, and Ministerio de Ciencia e Innovación CONSOLIDER-INGENIO 2010 Program Grant CSD2008-00005 (to L. A. M.-C.). The authors declare that they have no conflicts of interest with the contents of this article.

♦ This article was selected as one of our Editors' Picks.

[‡] This article contains supplemental Figs. S1–S5 and Movies S1–S3.

The atomic coordinates and structure factors (codes 5LXQ and 5MMZ) have been deposited in the Protein Data Bank (<http://www.pdb.org/>).

¹ Both authors contributed equally to this work.

² Supported by the Canadian Institute for Health Research Operating Grant 343439 (to M. L. T.).

³ Supported by Collaborative Research Grant 12.01.134/2bT4 from the Berlin Institute of Health.

⁴ Supported by Grant P11-CTS-07187 from Junta de Andalucía (Spain).

⁵ Supported by Grant PI14/00760 from Fondo de Investigación Sanitaria, Spain, co-financed by the European Regional Development Fund, "A Way to Build Europe."

⁶ To whom correspondence may be addressed. E-mail: Dominik.Mueller@charite.de.

⁷ To whom correspondence may be addressed. E-mail: Michel.tremblay@mcgill.ca.

⁸ To whom correspondence may be addressed: Structural Biology Unit, Center for Cooperative Research in Biosciences (CIC bioGUNE), Bizkaia Science and Technology Park Bldg. 800, 48160-Derío, Bizkaia, Spain. Tel.: 944-061-320; Fax: 944-061-301; E-mail: amartinez@cicbiogune.es.

The phosphatases of regenerating liver (PRLs),⁹ consisting of PRL-1, PRL-2, and PRL-3, are members of the PTP family. These three closely related PTPs are small single-domain enzymes of ~20 kDa that share about 80% amino acid sequence identity (supplemental Fig. S1) (1) and have a prenylation sequence at the C terminus, which seems to guide their localization in the endosomal compartment and at the plasma membrane (2). The PRLs are highly expressed in the majority of human solid tumors, as well as hematological cancers, and are considered the most oncogenic of all PTPs (3, 4).

⁹ The abbreviations used are: PRL, phosphatase of regenerating liver; CNNM, cyclin M; CBS, cystathionine β -synthase; PTP, protein tyrosine phosphatase; PDB, Protein Data Bank; ITC, isothermal titration calorimetry; AU, asymmetric unit.

PRL-1 was first identified as an immediate early gene in regenerating liver after partial hepatectomy (5), and it has recently been shown to be important for liver regeneration (6). Also, increased expression of this PTP has been associated with cell proliferation, invasion, and migration in various cell types (7–10). The oncogenic role for PRL-1 in cancer progression was further strengthened by the observation that its expression level is increased during tumor progression (10–12) implicating PRL-1 as a potential prognostic marker as well as therapeutic target in cancer. PRL-1 crystal structure analysis revealed a shallow active-site pocket that is characteristic of dual specificity phosphatase (phosphatases that can act upon tyrosine and serine/threonine residues) (13, 14). Furthermore, this PTP exists as a trimer in the crystalline state, and this could potentially regulate its function as well as its membrane localization (7, 13, 14). Interestingly, the active-site residue Cys-104 was found to form a disulfide bond with a nearby residue Cys-49, suggesting a potential mechanism for redox regulation (14, 15). Functionally, no direct substrate has yet been identified for PRL-1, but it has been associated with the regulation of several signaling pathways (16).

Despite an increasing number of PRL-related studies, their exact mechanisms of oncogenic transformation or normal physiological function were not well understood until recently, when a new paradigm was uncovered showing that PRLs regulate magnesium transport via their binding to magnesium transporters of the cyclin M (CNNM) family (17). This association was independently found by other authors (18), confirming that the association of PRLs with CNNMs causes a rise in intracellular magnesium levels that promote cancer progression (17, 18).

In recent years, the existence of specific genes encoding proteins directly involved in the transport of magnesium through cell membranes has been uncovered (19). This includes the human “CBS domain divalent metal cation transport mediator” (CNNM) gene family, also referred to as ancient conserved domain proteins (20–22), that include four isoforms (CNNM1–4) that are expressed in all human tissues (20) except for CNNM1, which is mainly expressed in the brain (23, 24). Mutations in CNNM2 cause familial dominant hypomagnesemia (MIM613882) (23, 25) and have been recently linked to major neuropsychiatric disorders (26), intellectual disability, and disturbed brain development (27). In contrast, mutations in CNNM4, the closest homolog of CNNM2, are considered the cause of the autosomal-recessive cone-rod dystrophy with amelogenesis imperfecta (MIM217080) (28, 29). Although it is well recognized that CNNM family members control intracellular magnesium levels, there is a debate about their activity as either efflux (18) or influx (17) transporters or, alternatively, as sensors (23) or homeostatic factors (30) that indirectly regulate transcellular Mg^{2+} transport. Importantly, recent findings highlight essential roles of the CNNM family, such as regulation of the circadian rhythm (31) and reproduction (32).

Structurally, CNNMs are complex proteins that contain an extracellular N-terminal domain preceding a DUF21 transmembrane domain (Pfam code PF01595), a “Bateman module” (33–35), and a C-terminal cNMP (cyclic nucleotide monophosphate) binding domain (Pfam code PF00027) (supplemental

Fig. S2) (36). We recently found that the Bateman module of CNNM2, consisting of two consecutive CBS domains, associates itself with disc-like dimers commonly referred to as “CBS modules” (supplemental Fig. S2) that accommodate nucleotides and metal ions (37, 38). In the absence of bound nucleotide, the CBS module adopts a Y-shaped or “twisted” conformation (PDB code 4IYS) (supplemental Movie S1), where the interfacial helices H3 and H4 maintain the CBS2 domains from complementary subunits in close contact with each other, although the CBS1 domains are separated (37). Upon binding of phospho-nucleotides (AMP, ADP, ATP, and MgATP), a network of polar interactions centered around Thr-568 is disrupted, thus causing a coordinated reorientation of helices H0 and H4 (supplemental Fig. S2), concomitant to a relative rotation of the two CBS motifs (37). This apparently smooth displacement of secondary elements within the subunit induces a dramatic structural change in the dimeric disc that evolves toward a “flat” arrangement (PDB codes 4P1G, 4IY0, and 4P1O) (supplemental Movie S2) in which both CBS1 domains interact symmetrically (37). Importantly, the conformational change in the CBS module is believed to be transmitted to the transmembrane region through the C-terminal α -helix H0 connecting both Bateman modules with the transmembrane domains, thus putatively modulating the activity of CNNM2 and its ability to regulate Mg^{2+} homeostasis (37). Remarkably, mutation of Thr-568 to isoleucine, as found in patients suffering from familial dominant hypomagnesemia (23), mimics the structural effect of nucleotide binding and stabilizes the flat conformer, thus impairing the conformational equilibrium of CNNM2, which becomes “locked” in a nucleotide-bound-like (non-functional) state (37). The high sequence conservation shared by all CNNMs in the Bateman module regions (supplemental Fig. S1) suggests that a similar behavior might be followed by other members of the family.

Interestingly, the Bateman module in CNNM3 mediates PRL-2 binding via an extended loop from the second CBS domain (17) (an alignment showing the sequence similarity in this region across the CNNM members as well as its spatial position is shown in supplemental Figs. S1 and S2). This loop is highly conserved in all CNNM family members across species, and phylogenetic analysis revealed that it is present only in species that contain PRL orthologs (17).

Here we report that, besides phosphonucleotides and metal ions, the Bateman module of CNNM2 can associate with each of the three human PRLs to form stable complexes where each molecule is structurally modified. We further describe the crystal structure of one of these complexes, PRL-1·CNNM2_{BAT}, both in the absence and in the presence of bound ATP and Zn^{2+} ions.

Our data reveal the key residues participating in the interaction between these two proteins and show the structural rearrangements that occur upon complexation, thus providing the structural basis for the oncogenic association between the PRL-1 phosphatase and CNNM2. Finally, we propose the molecular mechanism by which this partnership raises the intracellular Mg^{2+} content of cancer cells thus contributing to tumor growth and the acquisition of oncogenic properties (17).

Structure of PRL-1 in Complex with CNNM2

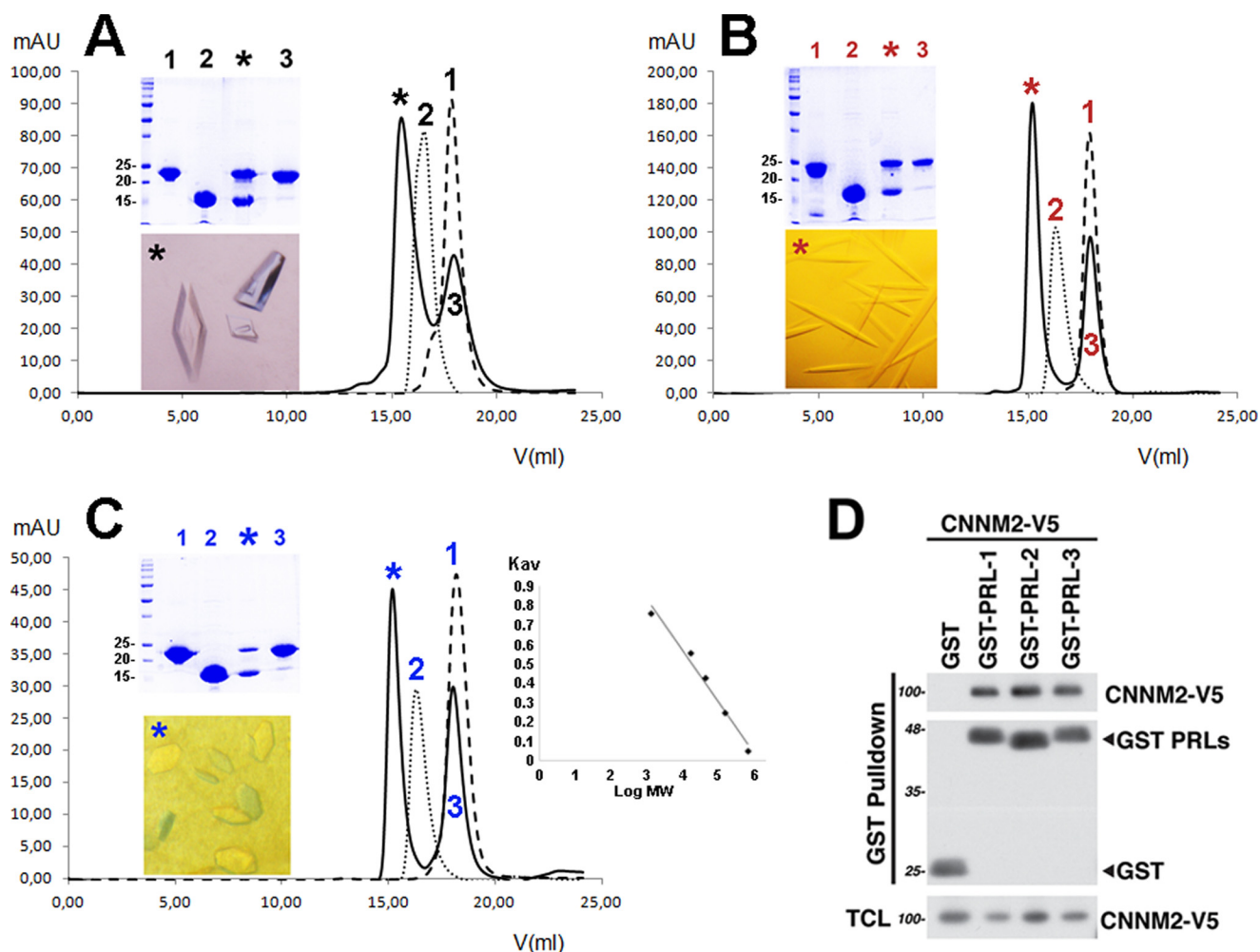


FIGURE 1. CNNM2_{BAT} interacts with all PRLs. A–C, size exclusion chromatography was used to isolate the corresponding PRLs·CNNM2_{BAT} complexes. Pure PRL-1, -2, and -3 (peak 1; $M_{th} = 22.6, 21.9,$ and 22.4 kDa, respectively (where M indicates mass)) eluted as monomers ($V_e \approx 17$ ml; $M_{exp} \approx 13$ – 15 kDa) when they were independently loaded into a size exclusion chromatography column. In the absence of PRLs, CNNM2_{BAT} (peak 2; $M_{th} \approx 34$ kDa) eluted as a dimer ($V_e \approx 16$ ml; $M_{exp} \approx 25$ kDa) (37, 39). The molecular masses of the resulting PRL-1/-2/-3·CNNM2_{BAT} complexes ($M_{th} \approx 40$ kDa; marked with black, red and blue asterisks, respectively) were consistent with $2 \times \text{PRL} + 2 \times \text{CNNM2}_{\text{BAT}}$ heterotetramers in solution ($V_e \approx 14.7; 14.5$ and 14.5 ml, respectively; $M_{exp} \approx 43, 48,$ and 48 kDa, respectively). The calibration trendline is $y = -0.2451x + 1.5726$ ($y = K_{av}; x = \log M$). Peak 3 arises from the excess of PRL protein present in the incubation solution. The corresponding bands in the SDS-polyacrylamide gels are shown on the left of each plot. Bands 1 and 2 correspond to independent chromatographic runs of pure CNNM2_{BAT} (M_{th} /subunit ≈ 18 kDa) and PRLs proteins. M_{th} and M_{exp} represent the theoretical and experimental molecular mass values, respectively. In agreement with the crystal data, the densitometry analysis (using the ImageJ gel analysis tool; rsb.info.nih.gov) of the two bands obtained in the wells marked with black, red, and blue asterisks showed a PRL-to-CNNM2_{BAT} ratio of 1.03, 0.97, and 0.95, respectively. The crystals of the PRL-1, -2, and -3·CNNM2_{BAT} complexes shown on the left of each plot, diffracted X-rays to a resolution of 2.4, 7.0, and 11 Å, respectively. D, pull-down experiments of V5-tagged full-length CNNM2 with GST-tagged PRL-1, -2, or -3 show the ability of CNNM2 to interact with the three PRL members. HeLa cells were transiently co-transfected with V5-tagged CNNM2 (CNNM2-V5) and GST-tagged PRL-1, -2, or -3 for 24 h. GST pull-downs (PD GST) were immunoblotted with V5 and GST antibodies. TCL, total cell lysate.

Results

CNNM2 Associates with All Three PRLs—The association of PRLs with the CNNMs has been demonstrated to control the intracellular magnesium levels, but whether all PRL members have the same mechanism of action still remains to be elucidated. Based on previous findings showing that all PRLs interact with CNNM3 (17) and CNNM4 (18), and by taking into account the close sequence homology (supplemental Fig. S1) and possibly similar functions shared by CNNMs, we first assessed whether CNNM2 interacts with all three PRL members.

In this study, we used the full-length human PRL proteins and an engineered protein construct, CNNM2_{BAT} (39), comprising residues 429–584 and containing the Bateman module of CNNM2 and the preceding α -helix (H0) that connect to the

DUF21 transmembrane domain (supplemental Figs. S1 and S2). We found that the three potential PRLs·CNNM2_{BAT} complexes are indeed formed (Fig. 1). In apparent contradiction with former observations describing PRL-1 as a trimer in solution (13), but in agreement with NMR experiments showing that PRL-3 exists in a monomeric state (40), PRL-1 eluted as a monomer in all our size exclusion chromatography experiments. In contrast, pure CNNM2_{BAT} eluted as a dimer (Fig. 1), as we described previously (37). The equivalent PRL-2·CNNM2_{BAT} and PRL-3·CNNM2_{BAT} complexes behaved similarly (Fig. 1). Additional experiments co-transfecting V5-tagged full-length CNNM2 and GST-tagged PRL-1, -2, and -3 in HeLa cells, followed by GST pull-down, supported the ability of CNNM2 to bind all PRL members (Fig. 1).

TABLE 1

Data statistics and refinement

One crystal was used per data set. Values in parentheses are for the highest resolution shell. NA = not applicable.

Proteins	PRL-1 + CNNM2 _{BAT}	PRL-1 + CNNM2 _{BAT} + ATP Zn ²⁺
Data collection and process		
Beamline	ALBA, XALOC	ESRF ID23.1
Radiation wavelength (Å)	0.9795	1.2837
Space group/PDB code	I222/5MMZ	C2/5LXQ
<i>a</i> (Å)	52.7	166.9
<i>b</i> (Å)	128.5	125.6
<i>c</i> (Å)	153.9	61.0
Molecules per AU	1 × (PRL-1 + CNNM2 _{BAT}) (1 heterodimer)	2 × (PRL-1 + CNNM2 _{BAT}) (1 heterotetramer)
Resolution (Å)	98.6–2.4 (2.41–2.40)	47.9–3.3 (3.34–3.33)
<i>R</i> _{sym} ^a	0.054 (1.151)	0.091 (1.120)
<i>R</i> _{meas} ^b	0.056 (1.197)	0.099 (1.221)
<i>R</i> _{pim} ^c	0.016 (0.327)	0.038 (0.478)
No. of observations	271,410	119,978
No. of unique reflections	20,944	17,868
Mean <i>I</i> / σ <i>I</i>	26.5 (2.5)	13.9 (1.7)
<i>CC</i> _{1/2}	0.99 (0.86)	0.99 (0.63)
Completeness (%)	99.8 (86.0)	99.9 (97.9)
Redundancy	13.0 (13.5)	6.7 (6.3)
Mosaicity (°)	0.2	0.2
Refinement statistics		
No. of working/test reflections	20,921/1019	15,312/1540
<i>R</i> _{work} ^d / <i>R</i> _{free} ^e	0.23/0.25	0.20/0.23
No. of atoms		
Protein	2299	4648
Ligand	NA	62 (2 × ATP)/2 (zinc)
Water	7	NA
Average B factors (Å ²)		
Protein	78.4	70.7
Ligand	NA	47.5 (ATP)/81.8 (zinc)
Water	73.9	NA
Room mean square deviations		
Bond lengths (Å)/angles (°)	0.003/0.804	0.001/1.255
Ramachandran plot statistics (%)		
Residues in most favored regions	97.6	97.3
Residues in additional allowed regions	2.4	2.7
Residues in disallowed regions	0	0

$$^a R_{\text{sym}} = \frac{\sum_{hkl} \sum_i |I_i(hkl) - \langle I(hkl) \rangle|}{\sum_{hkl} \sum_i I_i(hkl)}$$

$$^b R_{\text{meas}} = \frac{\sum_{hkl} \sum_i |I_i(hkl) - \langle I(hkl) \rangle|}{\sum_{hkl} \sum_i I_i(hkl)}$$

$$^c R_{\text{pim}} = R_{\text{pim}} = \frac{\sum_{hkl} \sum_i |I_i(hkl) - \langle I(hkl) \rangle|}{\sum_{hkl} \sum_i I_i(hkl)}$$

$$^d R_{\text{work}} = \frac{\sum |F_o - F_c|}{\sum F_o}$$

$$^e R_{\text{free}} = \frac{\sum |F_o - F_c|}{\sum F_o} \text{ calculated using a random 5\% of reflections that were not included throughout refinement.}$$

Structure of the PRL-1·CNNM2_{BAT} Complex—The three PRL·CNNM2_{BAT} complexes could be isolated and crystallized, but only those crystals containing PRL-1 showed suitable properties for a crystallographic analysis (Fig. 1). The lattice parameters, merging statistics, and the systematic absences obtained from the PRL-1·CNNM2_{BAT} crystals were consistent with space group *I*222, with one PRL-1·CNNM2_{BAT} heterodimer per asymmetric unit (AU) (Table 1). The application of the symmetry operations to the AU revealed the biological unit, a 2 × PRL-1·2 × CNNM2_{BAT} heterotetramer with elongated shape that contains one central disc-shaped homodimer of CNNM2_{BAT} subunits (also known as “CBS module” (34, 35)) bound to two independent PRL-1 molecules, each one located at opposite tips of the disc (Fig. 2 and supplemental Movie S3). The interaction between the CNNM2_{BAT} subunits (that are related by a crystallographic 2-fold axis) occurs through their interfacial α -helices (H1, H2, H3, and H4) and buries a surface of 1416 Å², whereas the CNNM2_{BAT}/PRL-1 interface buries 491 Å². The two PRL-1 proteins do not interact with each other.

The association of CNNM2 with PRL-1 induces structural re-arrangements in both proteins. In CNNM2, the most significant changes affect the extended L553–559 (linking strands β 5 and β 6 (Fig. 2)), which becomes ordered by entering into the catalytic cavity of PRL-1 (Fig. 3). The exposed and elongated

shape of this loop, as well as the relevance of its location, suggest that it might be the first anchor point between the two proteins when they begin to contact. In support of this, we found that a single point mutation (D558A) of the critical amino acid of CNNM2 that enters the catalytic cavity of PRL-1 completely disrupts PRL-1·CNNM2 complex formation (Fig. 3). In contrast, the independent substitution of residues located at strands β 4 and β 5 of CNNM2 by an alanine, threonine, or asparagine (F526A, D528A/D528N, V551A/V551T, or N553A/N553T) is not sufficient to block the formation of the complex, thus suggesting a secondary role for these residues in the interaction between the two proteins (Fig. 3 and supplemental Movie S3). Of note, a single substitution of the conserved glycine at position 565, located at the middle of β 6 (supplemental Fig. S1), weakens the protein/protein interaction, probably by causing a disorientation of strand β 6 (Fig. 3) that is transmitted to the preceding region of the polypeptide chain. These data enhance the key role played by L553–559 and are in agreement with our recent observations demonstrating that substitution of Asp-426 in CNNM3 (homolog of Asp-558 in CNNM2) results in losing the ability of this protein to interact with PRL-2 (41). Interestingly, the overexpression of the CNNM3 D426A mutant in cancer cells is known to decrease their ability to proliferate under magnesium-deprived situation, demonstrating a

Structure of PRL-1 in Complex with CNNM2

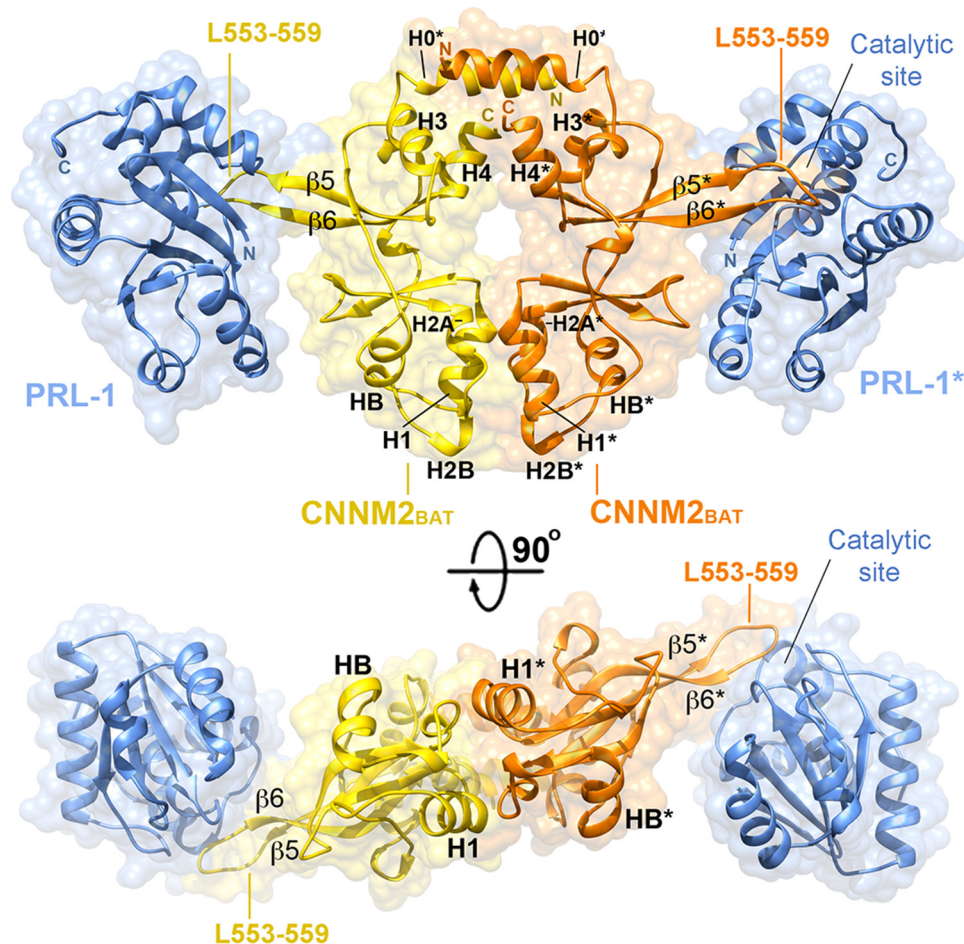


FIGURE 2. **Crystal structure of the PRL-1-CNNM2_{BAT} heterotetramer.** The structure consists of a flat CBS module (a disc-shaped dimer of CNNM2_{BAT} subunits, in *yellow* and *orange*, respectively) (37) associated with two independent PRL-1 molecules (in *blue*). Loop 553–559, connecting strands $\beta 5$ and $\beta 6$, interacts with residues located at the catalytic cavity of PRL-1. The secondary elements of the second molecule are indicated with *asterisks*.

PRL-2-CNNM3 complex-dependent oncogenic advantage in a more stringent environment (41). However, the main changes occurring in PRL-1 are in loops configuring the walls of the catalytic cavity as follows: the P-loop (residues 103–110), the WPD-loop (residues 68–77), the TI-loop (residues 137–143), and the $\beta 3\alpha 2$ -loop (residues 48–55) (Fig. 3). PRL-1 shares the HCX₅R active site, the P-loop, and the WPD-loop motifs typical of PTPs (14, 42), and its strong structural similarity to dual specificity phosphatases (DSPs) suggests that it is able to dephosphorylate both tyrosine and serine/threonine residues (14, 42). In the complex, and similarly to when substrates or substrate analogs (*e.g.* SO₄²⁻) are bound into the catalytic cavity of PRL-1 (13), the P- and WPD-loops collapse toward the cleft and interact with L553–559 of CNNM2 (Fig. 4). This closed conformation presumably prevents the access of substrates and explains why the phosphatase activity of PRL-1 measured *in vitro* is significantly reduced in the presence of CNNM2_{BAT} (Fig. 4).

Interestingly, the conserved Arg-110 at the HCX₅R motif of the P-loop shifts toward residue Asp-72, as when substrates are bound to the catalytic cavity (Fig. 5). The guanidinium group atom of Arg-110 forms a salt bridge with Asp-558, which is buried in the catalytic cavity near the substrate site. Thus, residue Arg-110 plays an important role by interacting with the catalytic Asp-72 of the WPD-loop, and it neutralizes the other-

wise electrostatic repulsion that would occur between Asp-72 and Asp-558 (CNNM2) upon formation of the complex. The overall network of interactions contributes to maintaining the WPD-loop in a substrate-bound-like conformation (Fig. 5). Noteworthy, the presence of residues Gly-73 in the WPD-loop of PRL-1 and Gly-557 in the L553–559 loop of CNNM2, together with a proline at position 559 in CNNM2, allows a tighter approximation between the two proteins. Another relevant interaction involves hydrophobic residues of the P-loop of PRL-1 (Val-105, Ala-106, Leu-108 and the alkyl chain of Arg-110) and of the L553–559 loop of CNNM2 (Pro-559, Phe-560, and Tyr-561). Residues Ala-140, Pro-7, and Phe-141 of PRL-1 (Fig. 3) also contribute to this hydrophobic environment. However, the catalytic cysteine at position 104 forms a sulfur bridge with Cys-49 (Fig. 3), suggesting that the interaction between these two residues does not play a key structural role in the stability and/or formation of the complex.

The interaction between CNNM2 and PRL-1 is not limited to the L553–559 loop and the PRL-1 catalytic cavity but involves additional elements. The CNNM2-PRL-1 interface involves residues from the C-terminal end of strands $\beta 4$ (Phe-526) and $\beta 5$, L553–559, and the N terminus of strand $\beta 6$ of CNNM2. Regarding PRL-1, it involves residues from the last turn of helix $\alpha 5$ (residues 134 and 135), loop $\alpha 5$ - $\alpha 6$ (136–142), and the first

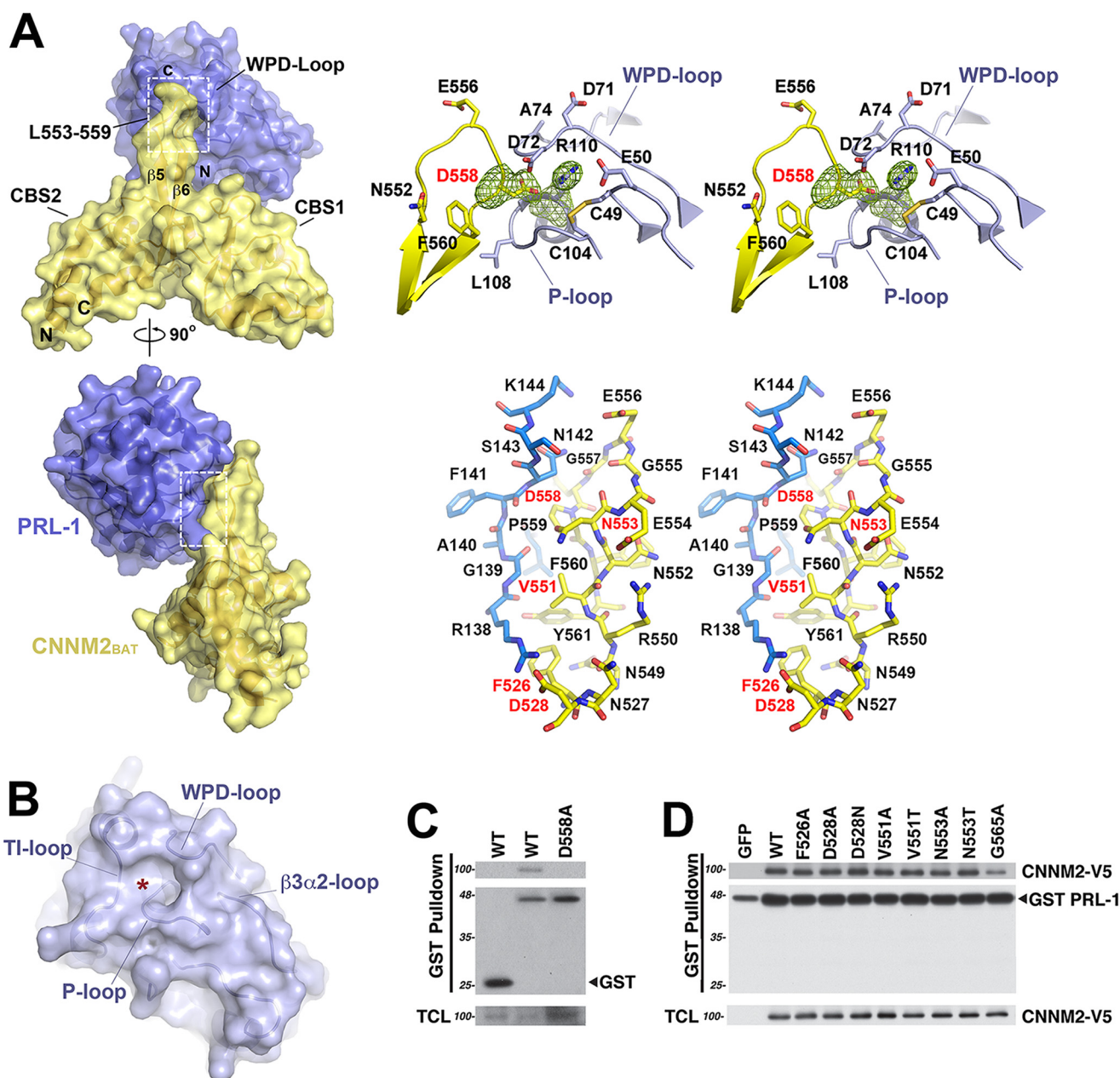


FIGURE 3. PRL-1-CNNM2_{BAT} interface. *A, left*, representation of the molecular surface of CNNM2_{BAT} (yellow) and PRL-1 (blue). The main amino acid residues involved in protein/protein interactions (white frames) are represented with sticks on the right. Of note, Asp-558 of CNNM2 enters into the catalytic cavity of PRL-1 and occupies the location of substrate analogs (e.g. SO_4^{2-}). This appears to promote the closure of the P- and WPD-loops of PRL-1 (see Fig. 5). Electron density evidence for Asp-558 and Arg-110 is shown in the unbiased omit $F_o - F_c$ density map contoured at 3.0σ . *B*, surface representation of PRL-1 showing the four loops configuring its catalytic cavity (highlighted with an asterisk). The coordinates of PRL-1 are extracted from the PRL-1·CNNM2_{BAT} complex described in this work. *C*, single mutation D558A completely abolishes complex formation. HeLa cells were transiently co-transfected for 8 h with GST alone or GST-PRL-1 in presence of the full-length CNNM2-V5 (WT) or CNNM2 D558A-V5 mutant (D558A). GST pulldown was performed on cell extracts followed by Western blotting analysis with either V5 or GST antibodies. *D*, single point mutation of residues Phe-526, Asp-528, Val-551, or Asn-553 (located at the protein/protein interface and highlighted in red) by an alanine or threonine is not sufficient to block complex formation. HeLa cells were transiently co-transfected for 24 h with GST alone or GST-PRL-1 in the presence of either the full-length CNNM2-V5 (WT) or various point mutants. GST pulldown was performed on cell extract followed by Western blotting analysis with either V5 or GST antibodies. GFP and GST were used as negative controls. TCL, total cell lysate.

turn of helix α_6 (Ser-143 and Lys-144), the central residues of the WPD-loop (residues 71–73) and P-loop (residues 106–198), and in a minor extent the residues configuring the N-terminal end (Pro-7) (Fig. 3). Importantly, residues Arg-138 (at the beginning of loop α_5 - α_6) and Lys-144 of PRL-1 form salt bridges with residues Asp-528 (located in the loop that precedes helix H3 in CNNM2) and Glu-556 (at the tip of L553–559), respectively. Additionally, Arg-138 H-bonds Asn-527.

The alkyl chain of Arg-139 of PRL-1 contributes to the hydrophobic environment participated in by Tyr-561 and Phe-526 of CNNM2.

cNMP Domain of CNNM2 Is Not Involved in the PRL-1/CNNM2 Interaction—The participation of apparently few structural elements from CNNM2 in the PRL-1·CNNM2_{BAT} complex, prompted us to investigate the possible implication (if any) of the C-terminal cNMP domain of the transporter in

Structure of PRL-1 in Complex with CNNM2

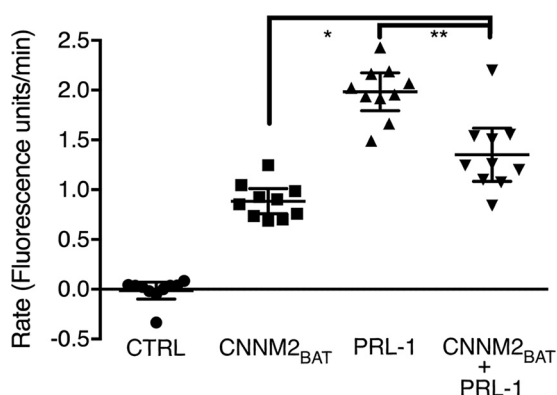


FIGURE 4. CNNM2_{BAT} decreases the enzymatic activity of PRL-1. 15 μg of His-CNNM2_{BAT} and 15 μg of His-PRL-1 were tested either alone or in combination after 30 min of incubation along with a buffer control (CTRL) (0.1 mg/ml BSA, 3 mM DTT, 50 mM HEPES, pH 7.0, NaOH). The enzymatic activities were evaluated by measuring the rate of hydrolysis of a fluorescent synthetic substrate (6,8-difluoro-4-methylumbiliferyl phosphate). To see this enzymatic activity, 50 μM DiFMUP was used. This experiment was done twice; the results were pooled ($n = 10$), and they are represented as mean \pm 95% confidence interval with two-way analysis of variance using CNNM2_{BAT} and PRL-1 as two factors ($p < 0.0001$) followed by Tukey's multiple comparison test with adjusted p values: *, $p < 0.001$; **, $p < 0.0001$.

the interaction between the two proteins. To that goal, two additional constructs containing the cNMP domain only (CNNM2_{cNMP}; residues 593–875) or the entire intracellular region (CNNM2_{BAT-cNMP}; residues 429–875) were evaluated in binding assays by means of isothermal calorimetry techniques (ITC). As shown in Fig. 6, binding signals were only observed when the CNNM2_{BAT} domain was present in the construct, with moderate and similar affinities ($K_D \approx 0.5 \mu\text{M}$) (Table 2). Either for CNNM2_{BAT} or CNNM2_{BAT-cNMP}, the binding is driven enthalpically ($-T\Delta S$ is virtually zero). The resemblance in the affinity and entropic/enthalpic signature suggests that the binding modes of these constructs to PRL-1 are structurally similar. In contrast, binding signals were very small or identical to those obtained in the blank titration for CNNM2_{cNMP}. Thus, our data suggest that CNNM2_{cNMP} does not participate in the formation of the PRL-1·CNNM2 complex, or, alternatively, that the interaction proceeds with very small heat exchange (and thus it is not detected well by ITC), which is unlikely because protein/protein interaction often leads to significant surface burial (and therefore, binding enthalpy). Interestingly, our ITC experiments show that CNNM2_{cNMP} does not interact with CNNM2_{BAT} suggesting that these two intracellular domains act as independent modules.

Binding of PRL-1 Flattens the CBS Module of CNNM2—Unexpectedly, the CBS module of CNNM2 adopts a flat disc conformation in the complex (Figs. 2 and 7 and [supplemental Movie S3](#)) instead of the Y-shaped twisted state ([supplemental Movie S1](#)) that one would expect in the absence of bound nucleotides and/or bound metal ions (37). This flat state is equivalent to that adopted in the presence of bound MgATP ([supplemental Movie S2](#)) or in the pathogenic T568I variant protein (37). The flat conformation found in the complex appears to be favored by the presence of electrostatic charges of opposite sign that, due to their strategic distribution along the surface of both proteins (Fig. 7), exert a mutual attraction that causes the dis-

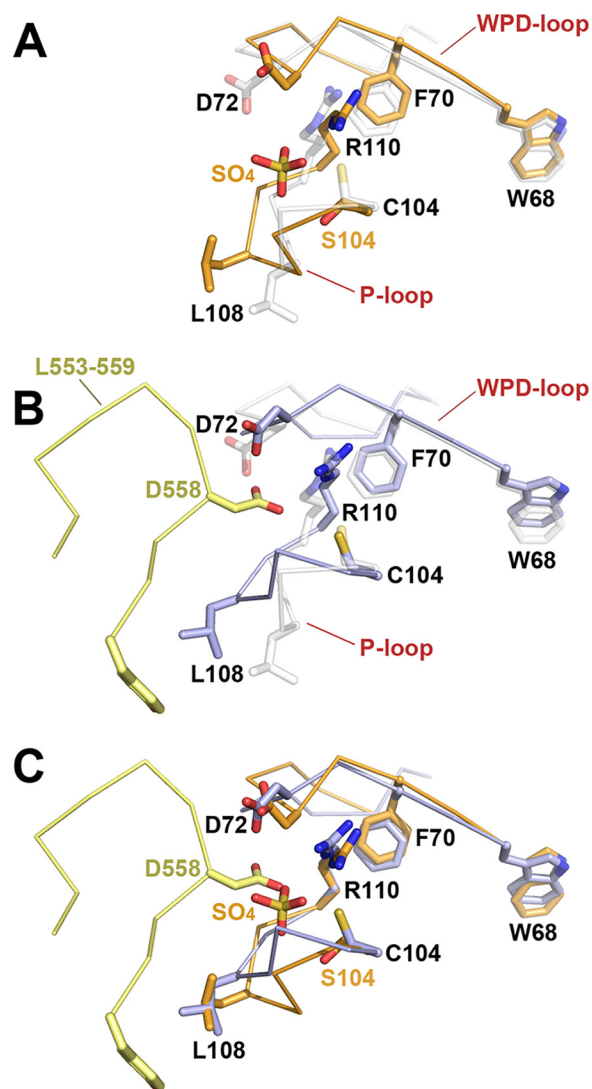
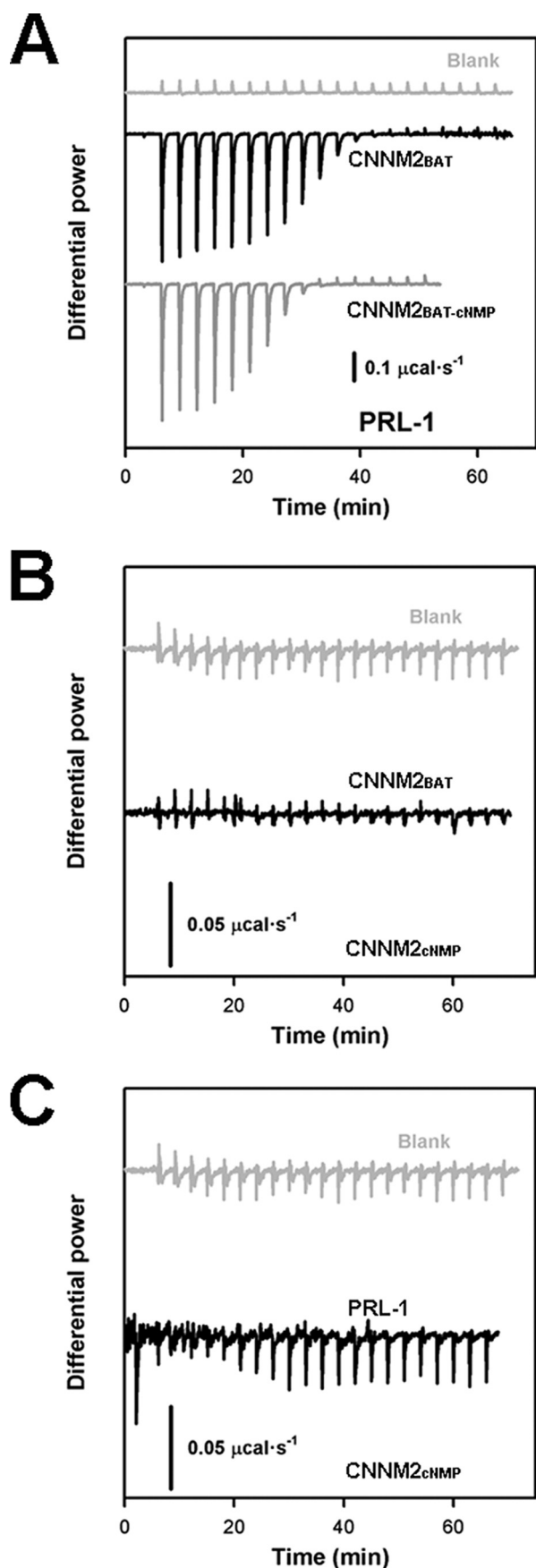


FIGURE 5. Effect of CNNM2 on PRL-1. *A*, superimposition of the WPD- and P-loops in apo-PRL-1 (light gray) and SO_4 -bound PRL-1 (orange). Both structures show the WPD-loop in a closed conformation collapsed toward the SO_4 -binding position. In contrast, the P-loop appears open and distanced from SO_4 in apo-PRL-1 but closed (and folded toward SO_4) in the SO_4 -bound complex. *B*, superimposition of the WPD- and P-loops in apo-PRL-1 (light gray) and in the PRL-1·CNNM2_{BAT} complex (light blue). The L553–559 of CNNM2 is in yellow. *C*, superimposition of the WPD- and P-loops in SO_4 -bound PRL-1 (orange) and in the PRL-1·CNNM2_{BAT} complex (light blue). Binding of CNNM2 exerts an effect on both loops that is similar to that of substrate binding. Residue Asp-558 from CNNM2 occupies a position similar to that of SO_4 .

placement of the CBS1 domain of CNNM2 toward the C-end of strand β_2 and the N-extreme of helix α_1 of PRL-1. Among the residues involved are Glu-462–Glu-485–Glu-487 and Lys-512–Lys-516 from CNNM2, and His-23–Asn-24–Asn-27 and Glu-35–Glu-36–Glu-61 from PRL-1. Our data suggest that binding of PRL-1 to the twisted conformation of the CNNM2_{BAT} dimer causes a concomitant shift of CBS1 domains (Fig. 7) from complementary subunits (37). This rearrangement alters the interactions between the interfacial helices linking the two Bateman modules in the CBS module, allowing it to progress from its twisted toward its flat state (37). Additionally, our data also indicate that because CNNM2 interacts with PRL-1 basically through the CBS2 domain, it is likely that the twisted-to-

**TABLE 2**

Thermodynamic binding parameters for the interaction between PRL-1 and CNNM2 constructs

Protein	<i>N</i>	<i>K_a</i> <i>10</i> ⁻⁶ (<i>M</i> ⁻¹)	<i>K_d</i> μ <i>M</i>	ΔH kcal·mol ⁻¹	$-T\Delta S$ kcal·mol ⁻¹
CNNM2 _{BAT}	2.02 ± 0.03	1.25 ± 0.01	0.64 ± 0.14	-8.9 ± 0.1	0.4
CNNM2 _{BAT-cNMP}	1.25 ± 0.01	2.0 ± 0.3	0.36 ± 0.04	-8.2 ± 0.1	-0.3

flat transition can proceed without altering the relative orientation between the two proteins.

Binding of ATP Induces Minor Changes in the PRL-1·CNNM2_{BAT} Complex—The former observations prompted us to explore whether binding of nucleotides and/or of divalent cations induce additional changes in the PRL-1·CNNM2_{BAT} complex, either promoting or preventing its formation. Based on the studies by Goytain and Quamme (22) showing that murine CNNM2 is a wide substrate selectivity transporter with the capability to transport Mg²⁺, Co²⁺, Mn²⁺, Sr²⁺, Ba²⁺, Cu²⁺, and Fe²⁺ ion, and on our own structural studies showing that CNNM2_{BAT} has the ability to bind AMP, ADP, and MgATP (37), we tried to grow crystals of the PRL-1·CNNM2_{BAT} complex in the presence of these potential substrates. Buffered solutions containing ATP and Zn²⁺ in acidic media yielded crystals of suitable quality for crystallographic studies. The presence of Zn²⁺ ions and ATP triggers subtle structural changes in the protein complex that result in a slightly different rearrangement of the molecules within the crystal, which belongs to the monoclinic *C2* space group (unit cell parameters: *a* = 166.9; *b* = 125.6; *c* = 61.0; β = 111.4°), and contain one 2×PRL-1·2×CNNM2_{BAT} heterotetramer per asymmetric unit (Table 1). In these crystals, the CNNM2_{BAT} subunits (and thus their bound ATP molecules) configuring the CBS module are related by a non-crystallographic 2-fold axis. As we had reported previously for the CBS module of CNNM2 alone (37), we found that ATP binds at site S2 of each Bateman module in the PRL-1·CNNM2_{BAT} complex (Fig. 8). Interestingly, the bound nucleotide barely induces structural changes with respect to the apo-form, the rearrangements being limited to a subtle approximation of the CBS1 motifs from complementary CNNM2_{BAT} subunits. These data indicate that substrates such as MgATP or ZnATP act in the same direction of PRL-1, thus reinforcing the structural change induced by the phosphatase. Upon completion of the refinement, the structural statistics (bond lengths (Å)/angles (°), as well as *R_w*/*R_F* values) were in the acceptable range at this resolution (43) (Table 1).

In former studies, we showed that, at neutral pH and in the absence of divalent cations, the CNNM2_{BAT} domain catalyzes slow ATP hydrolysis to ADP, where the turnover is mainly limited by weak affinity for the nucleotide (37). We also demonstrated that the barrier to ligand entry is significantly reduced by Mg²⁺ co-binding and that a shorter polyphosphate chain in the nucleotide (with nominally less negative charge) favors the protein/ligand interaction, suggesting that negative charge

FIGURE 6. Binding assays. Titrations of CNNM2 proteins. *A*, raw titrations of buffer (blank), CNNM2_{BAT} (23 μM; residues 429–584), or CNNM2_{BAT-cNMP} (29 μM; residues 429–875) with PRL-1 (540 μM). *B*, raw titrations of CNNM2_{BAT} with CNNM2_{cNMP} (0.78 mM; residues 593–875). *C*, raw titrations of PRL-1 with CNNM2_{cNMP}. *B* and *C* share the same blank titration obtained after titration of buffer with a CNNM2_{cNMP} (0.78 mM) solution.

Structure of PRL-1 in Complex with CNNM2

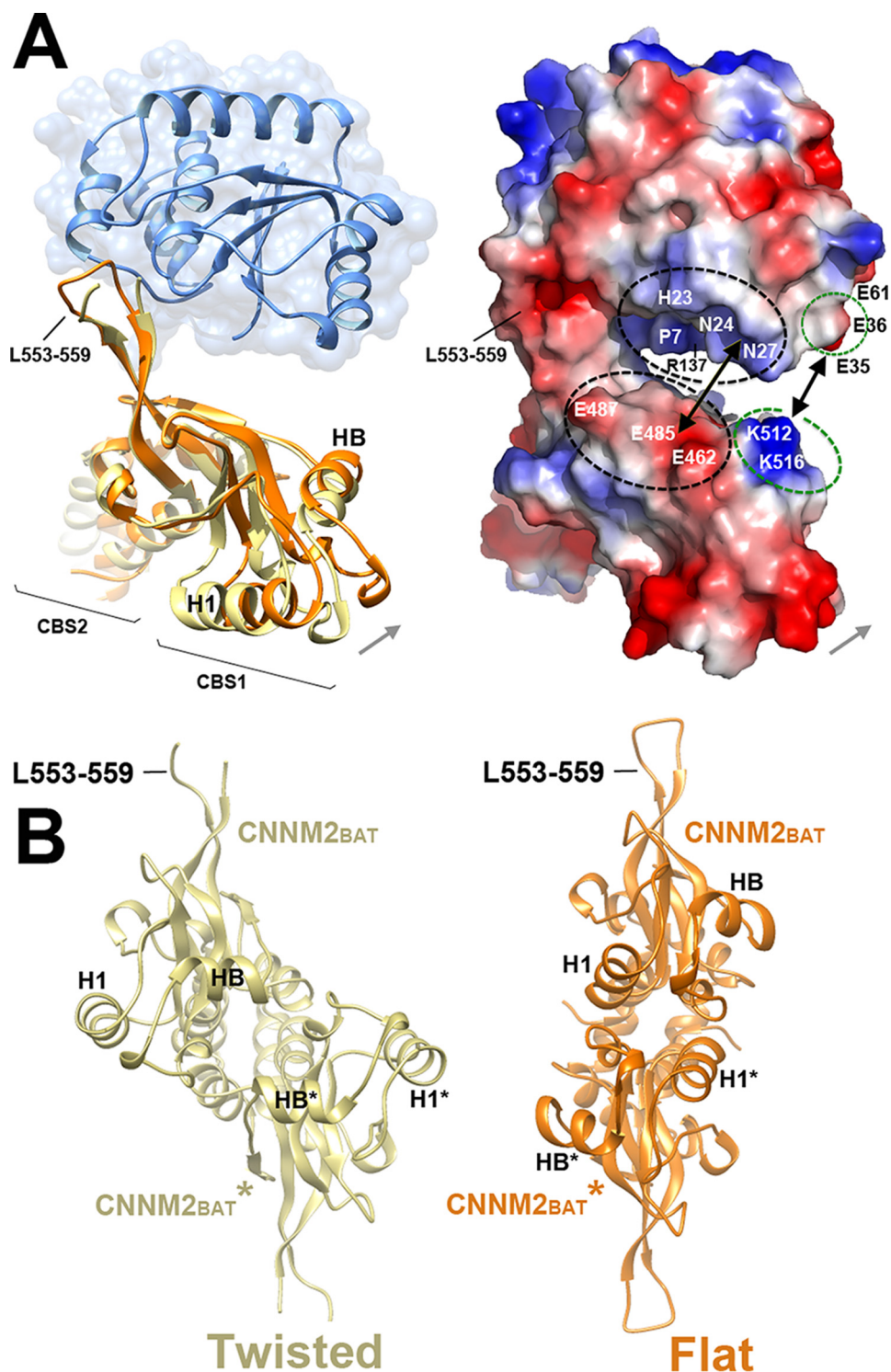


FIGURE 7. Effect of PRL-1 on CNNM2. *A, left*, structure of apo-CNNM2_{BAT} (37) (yellow) overlapped with PRL-1-CNNM2_{BAT} (PRL-1, cyan; CNNM2, orange). *Right*, representation of the molecular surface and electrostatic potential of PRL-1-CNNM2_{BAT}. Positively and negatively charged residues are in blue and red, respectively. Binding of PRL-1 to CNNM2_{BAT} causes a shift (indicated with an arrow) of the CBS1 domain that has a similar effect as that caused by MgATP (37). This structural rearrangement is favored by the electrostatic attraction between residues of opposite charge distributed along the surface of both proteins. *B*, such modification in each subunit makes the CBS module (dimeric association of two CNNM2_{BAT} subunits) progress from a twisted to a flat conformation (37).

repulsion between the acidic cluster formed by residues Glu-570, Asp-571, and Glu-574 at site S2 and the nucleotide's polyphosphate chain might play a major role in inhibiting ligand entry (37). These data prompted us to analyze the behavior of ATP in solution, both in the presence or in the absence of

the target proteins, to find out whether the hydrolysis phenomenon observed at pH 7 is reproduced (or not) under the current crystallization conditions, pH 4.6. To that aim, we monitored the hydrolysis of ATP by CNNM2_{BAT} and by the PRL-1·CNNM2_{BAT} complex, by means of ³¹P NMR. In a control with-

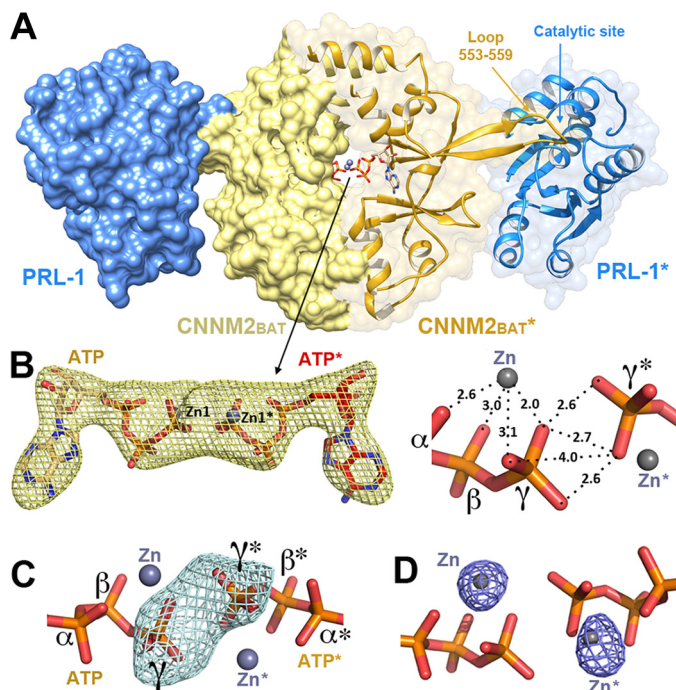


FIGURE 8. Structure of the PRL-1-CNNM2_{BAT} heterotetramer bound to ZnATP. *A*, two Bateman modules of CNNM2 (CNNM2_{BAT} and CNNM2_{BAT}^{*}, shown in *yellow surface and ribbons*, respectively) interact with two independent PRL-1 molecules (in *blue surface and ribbons*, respectively). One ZnATP molecule binds at site S2, located in the central cavity of each CNNM2_{BAT} subunit. *B*, ZnATP is shown in *balls-and-stick* model with the unbiased omit $F_o - F_c$ density map contoured at 3.5σ (in *light green*) resulting from omitting ZnATP prior to calculation of the map. The interatomic distances between the zinc atoms and the phosphate groups of ATP/ATP^{*} are shown on the *right*. *C* and *D* show the omit $F_o - F_c$ maps resulting from omitting the γ -phosphate moieties of ATP/ATP^{*} (cyan, contoured at 3.5σ) and Zn/Zn^{*} (blue, contoured at 8.0σ) prior to calculation of the maps.

out CNNM2_{BAT}, we found that ATP remained perfectly stable at pH 7 and 4.6 over at least 24 h, regardless of MgCl₂ or ZnCl₂ addition (supplemental Figs. S3 and S4). In the presence of CNNM2_{BAT} (50 μ M versus 1 mM ATP, pH 7), however, 50% of the ATP was hydrolyzed to ADP and free phosphate within 16 h (supplemental Fig. S3). No further processing of either ADP or AMP was observed. In agreement with former studies (37), addition of divalent cations strongly impeded ATP hydrolysis at pH 7. Within the same 16 h, only 20% ATP was hydrolyzed if MgCl₂ (5 mM) was added. Remarkably, Zn²⁺ (added as 5 mM ZnCl₂), but not Mg²⁺, completely stalled ATP hydrolysis by CNNM2_{BAT} either alone or bound to its partner protein PRL-1 (supplemental Fig. S3). Interestingly, the monovalent H₃O⁺ cation effected similar inhibition of ATP hydrolysis, with only 20% ATP hydrolyzed in 16 h if the pH was lowered from 7 to 4.6. At this elevated H₃O⁺ concentration, addition of MgCl₂ (5 mM) had no further inhibiting effect on ATP hydrolysis by CNNM2_{BAT}. The observation that increased cation concentrations (including H₃O⁺ at low pH) effectively hamper ATP hydrolysis by CNNM2 could be rationalized by charge compensation: In the absence of compensating cations, the high local negative charge density around two ATP molecules bound at close distance in the PRL-1-CNNM2_{BAT} heterotetramer might favor their partial hydrolysis to ADP with reduced negative charge. Cations bound in the vicinity would effectively screen the repulsive negative charges and thus reduce the pressure for

ATP hydroxylation. Our data also show that a cation-specific effect exists, as Zn²⁺ is a more potent inhibitor than Mg²⁺ or H₃O⁺. Briefly, neither CNNM2_{BAT} nor the PRL-1-CNNM2_{BAT} complex catalyze ATP hydrolysis to ADP and free phosphate in the presence of Zn²⁺ and/or in acidic media. Of note, both conditions are met by the crystallization buffer, thus explaining why intact ZnATP molecules (and not ADP or a mix of both nucleotides) are observed in our crystal structures.

In agreement with our NMR analysis, the unbiased omit $F_o - F_c$ maps resulting from omitting the entire nucleotide or the γ -phosphates confirmed the presence of two ATP molecules per CBS module (Fig. 8). Furthermore, the $mF_o - DF_c$ difference maps revealed residual density consistent with the presence of one Zn²⁺ ion bound to the α - and γ -phosphates of each ATP (Fig. 8). This Zn²⁺ ion (Fig. 8) matches the location of Mg²⁺ detected previously (37) and coincides with the position of Zn²⁺ atoms determined from anomalous difference maps obtained from crystals of CNNM2_{BAT} grown in the presence of ZnCl₂ (data not shown). Importantly, its positive charge reduces the electrostatic repulsion that otherwise would exist between the two neighboring ATP molecules and also between the nucleotide's phosphate moieties and the acidic cluster formed by residues Glu-570–Asp-571–Glu-574 at site S2 (37).

Discussion

Discovering the capacity of PRLs to interact with members of the CNNM family to increase the intracellular concentration of Mg²⁺ ([Mg²⁺]_i) and to promote tumor growth and metastasis has established an unprecedented link between cancer and Mg²⁺ homeostasis (17, 18). It has been observed that PRL-1, an important player for the regulation of cell cycle progression and proper timing of liver regeneration after partial hepatectomy (6), shows elevated levels in patients with hepatocellular carcinoma, and its ectopic overexpression markedly enhances hepatocellular carcinoma cell migration and invasion (10). Thus, PRL-1 is a potential prognostic marker as well as an attractive therapeutic target (10).

Interaction of PRL-1 with CNNM2 Alters the Structure of Both Proteins—A fact to note is that in forming the PRL-1·CNNM2_{BAT} complex, both proteins suffer structural modifications, although CNNM2_{BAT} is significantly more affected. This particular module appears to be the unique intracellular region that participates in the interaction with the phosphatase, and suffers a twisted-to-flat conformational change that determines the overall architecture of the protein complex. In contrast, PRL-1 barely varies its overall fold with respect to its uncomplexed state (Fig. 5 and supplemental Fig. S5). Upon binding to CNNM2, the P- and the WPD-loops configuring its catalytic cavity collapse toward the interior of the cleft and adopt a substrate-bound-like conformation (Fig. 5). Interestingly, the displacement of the WPD-loop observed in PRL-1 is not as drastic as that observed for PRL-3, which shows significant differences in this region (7, 13).

CNNM2 Binding Decreases PRL-1 Activity—As shown in Fig. 5, Asp-558 of CNNM2 occupies the position of substrate analogs of PRL-1 (13) in the PRL-1·CNNM2_{BAT} complex. This substrate analog-like role played by Asp-558, when entering the catalytic cavity of PRL-1, not only explains the rearrangement

Structure of PRL-1 in Complex with CNNM2

of the P-loop but also shed lights on the decrease in the already very weak phosphatase activity of PRL-1 observed *in vitro*. Yet, it also suggests a reciprocal role of CNNM2 on the regulation of PRL-1 that leads to cell proliferation likely through the rise of the important intracellular cation magnesium concentration.

The superimposition of PRL-1 with the structure of other phosphatases suggests that, despite being currently considered as a dual phosphatase, oncogenic PRL-1 is most probably a poorly active phosphoserine and/or threonine phosphatase, and not a phosphotyrosine phosphatase, because bulkier amino acids (*e.g.* phosphotyrosines) would likely avoid the interaction with its intracellular partner CNNM2. The lack of key catalytic residues in PRL-1 that are crucial in the phosphatase activity of highly active phosphatases like PTEN explains the very poor *in vitro* activity observed for PRLs (17). An example is the presence of an alanine (instead of a hydroxyl residue) next to the catalytic Arg-110 (44). In summary, the data presented here support recent findings claiming that the main role of PRLs might not be to dephosphorylate a variety of substrates but to interact with CNNMs to control their activity as magnesium transporters (17).

In light of our new structures, a new question arises on whether PRL binding affects and/or determines the affinity of interaction between CNNM2 and its ligands, such as Mg-ATP. The ability of PRL-1 to induce structural changes in CNNM2_{BAT} that are similar to those triggered by MgATP suggests that a prior binding of PRL-1 to CNNM2 might pre-configure site S2 for the subsequent accommodation of MgATP (thus, increasing the affinity of CNNM2 for this nucleotide). In contrast, one would not expect that a prior binding of MgATP to CNNM2 would increase the affinity of CNNM2 for PRL-1, because MgATP binding to CNNM2 does not significantly affect the orientation and/or the structure of L553–559 (the main anchoring point of CNNM2 to PRL-1).

The slight modifications observed in PRL-1 contradict a former hypothesis that significant rearrangements would likely occur in PRLs upon association with their physiological substrates (14). Previous data has pointed out that the functional unit of PRL-1 might be a trimer (13). However, our data clearly show that a trimeric assembly (13) would be sterically impeded in the PRL-1·CNNM2 complex, causing clashes with the surrounding CNNM2 molecules. These clashes would occur independently of the conformational state (twisted or flat) of CNNM2. Thus, if a functional PRL-1 trimer exists, disassembling of this species into its component subunits prior to (or during) its interaction with CNNM2 is an essential requisite in the molecular mechanism of Mg²⁺ transport.

PRL-1 Interacting Proteins—Only few PRL-1 interacting proteins have been identified so far. Among them are the aforementioned CNNM2, CNNM3 (17), and CNNM4 (18) transporters, the RhoA inhibitor p115 Rho-GTPase-activating protein (RhoGAP) (45), the nuclear transcription factor p53 (46), the activating transcription factor-5 (ATF-5 or ATFx), and α -tubulin (16). To our knowledge, the structural information is currently limited to the structure of PRL-1 bound to a peptide that shares high sequence identity with a conserved motif in the Src homology 3 domain of RhoGAP (45). As shown in Fig. 9, binding of CNNM2 to PRL-1 occurs at a distinct place of the Src

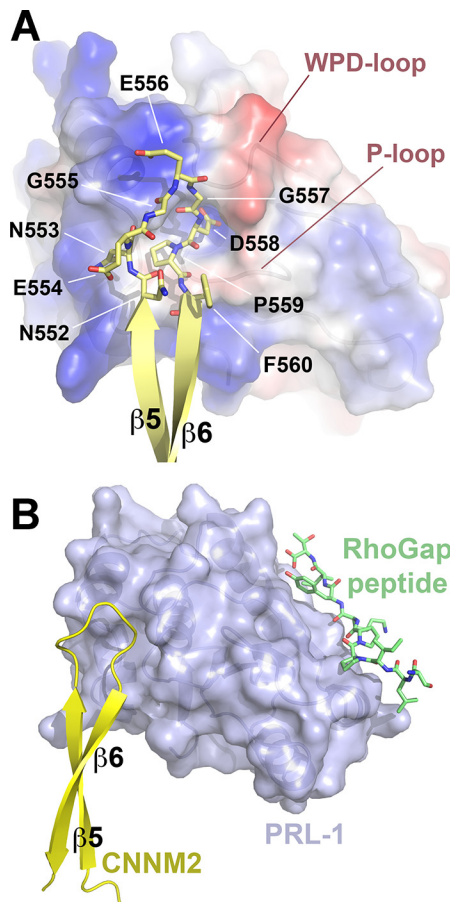


FIGURE 9. PRL-1 interacting proteins. *A*, representation of the molecular surface and electrostatic potential of the interaction face of PRL-1 with CNNM2. Positively and negatively charged residues are in blue and red, respectively. Residues Gly-555, Gly-557, and a Pro-559 in L553–559 provide sufficient flexibility to the main chain of CNNM2 to orient residues Glu-554, Glu-556, and Asp-558, toward positively charged areas of PRL-1. Residue Asp-558 from CNNM2 buries into the catalytic cavity of PRL-1 between the WPD- and P-loops. *B*, surface and ribbon representation of the interacting zone of PRL-1 (blue) with CNNM2 (yellow) and Src homology 3 domain of RhoGAP (green). As shown, CNNM2 and RhoGAP interact at opposite faces of PRL-1.

homology 3 domain of RhoGAP (PDB code 3RZ2) (45), suggesting a wide versatility of the PRL-1 surface to accommodate different partners.

Mechanism of Mg²⁺ Transport—With the structural data available so far, it is not yet possible to unequivocally assign the mode of transport (“on” or “off”), as well as the direction of the flux of ions through the membrane (in → out (efflux), or out → in (influx)) that corresponds to each of the two known conformations (twisted or flat) of the CBS module of CNNM2 (37). The structures of the PRL-1·CNNM2_{BAT} complex allow for attaching a few more pieces of this intriguing puzzle. At low [Mg²⁺]_i, the CBS module of CNNM2 does not bind Mg²⁺ and/or MgATP and adopts its twisted conformation (37) (*panel I*, Fig. 10). This structural state should correspond to a “transport-off” mode if CNNM2 behaves as a Mg²⁺ “importer” or an “importer regulator” in tumor cells, which is structurally in agreement with the structure-to-mode model that we postulated for CNNM2 at low [Mg²⁺]_i in the renal epithelia (37). However, it has been described that low [Mg²⁺]_i, or a higher demand of this cation in tumor cells, favors the expression of

Structure of PRL-1 in Complex with CNNM2

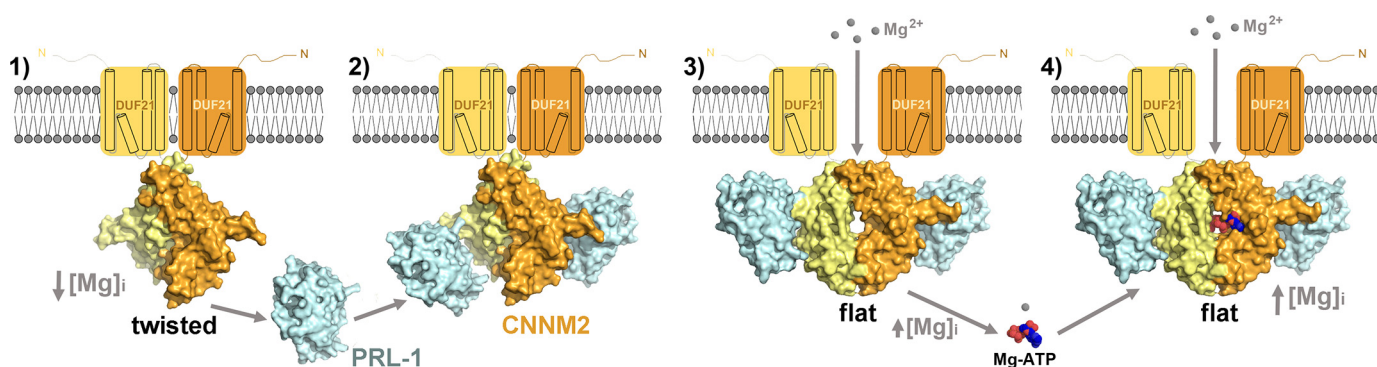


FIGURE 10. Postulated mechanism of Mg^{2+} transport in tumors is shown (panels 1 and 2). At low $[Mg^{2+}]_i$, or if magnesium is required by the cell, PRL-1 (in cyan) expression is increased and anchors to the twisted CBS module (yellow-orange) of CNNM2 (panel 3). Then, the electrostatic attraction between the surfaces of the two proteins flattens the CBS module, thus permitting the influx of Mg^{2+} into the cell (panel 4). The effect of PRL-1 on CNNM2 is complemented by a progressively increased $[Mg^{2+}]_i$, which results in binding of MgATP to the flat CBS module. Note: the structures represented in panels 1, 3, and 4 are extracted from the crystal structures of apo-CNNM2_{BAT} (PDB code 4IYS), PRL-1·apo-CNNM2_{BAT} (code 5CJK; 5MMZ is updated code), and PRL-1 + ZnATP-CNNM2_{BAT} (code 5LXQ), respectively. The structure of the PRL-1·CNNM2_{BAT(twisted)} complex represented in panel 2 is an *in silico* model created from apo-CNNM2_{BAT} (PDB code 4IYS) and apo-PRL-1 (PDB 5MMZ).

PRLs (17). Thus, as the number of PRL molecules increases, the PRL-1·CNNM2 complex would be formed gradually (panel 2, Fig. 10). Our new structural data suggest that, in the early stages, the nascent PRL molecules anchor to the L553–559 loop of CNNM2. Subsequently, the complementary charges distributed along the surfaces of both proteins (Fig. 7) would help to strengthen their interaction making the CBS module to progress from its twisted toward its flat state (Fig. 7). This conformational change would be transmitted to the DUF21 transmembrane domain through helix H0 from each subunit (Fig. 2) (37), thus allowing access of Mg^{2+} ions into the intracellular media (panel 3, Fig. 10). Concomitantly, an increased $[Mg^{2+}]_i$ favors its interaction with ATP and enhances the affinity of the latter for CNNM2 (panel 4, Fig. 10), thus contributing to maintaining the flat conformation and the “transport-on” state while Mg^{2+} consumption is demanded. Keeping in mind that the role of CNNM2 might differ in different cell types and tissues, it seems reasonable to assume that each of the conformations of CNNM2 may correspond to a unique state of transport, either “on” or “off,” but not to two of them. Thereby, the twisted and flat conformations are only consistent with an off and an on state, respectively, if CNNM2 works favoring Mg^{2+} efflux in the renal epithelia (37), although the influx of this cation is in the tumor cell. With the lack of further data, the available structures suggest that CNNM2 might play a dual role, thus allowing a bidirectional flux of Mg^{2+} ions depending on the cell type and tissue.

Structural Basis for Therapeutic Intervention—The presented data lead us to hypothesize that the design of peptides with an amino acid sequence similar to that of the extended loop of CNNM2 might be a useful tool to impair the association of PRL-1 with CNNM2, and it represents a potential strategy for drug design in cancer treatment. We should note that the participation of an extended loop in protein/protein interactions is not restricted to the CNNM family and has been formerly observed in other CBS domain-containing proteins such as human cystathionine β -synthase, where this structural element links the last two β -strands of the CBS2 domain and is key to maintaining the tetrameric assembly of the enzyme (47). Considering the sequence similarity shared by all members

of the PRL family and also across the CNNM proteins, the therapeutic approach mentioned above might be potentially extended to the rest of PRL members. In support of this, we found that the single substitution of the conserved aspartate residue located at the tip of the extended loop in at least two members of the CNNM family (Asp-558-CNNM2; Asp-426-CNNM3) has similar consequences and completely abolishes the CNNM/PRL interaction (Fig. 3) (41).

Because magnesium is an essential intracellular cation regulating numerous cellular functions, we believe that the elucidation of the PRL-1·CNNM2 complex presented here represents an important step to a better understanding of the physiological role of magnesium. In addition, it provides a molecular basis to decipher the function of the PRLs on how their recruitment by the CNNMs regulates their respective activities, modulates nucleotide binding, and affect magnesium transport in normal or tumor cells. This first elucidation of a PRL-CNNM complex should help to understand the relation between magnesium homeostasis and cancer.

Experimental Procedures

Expression and Purification of CNNM2_{BAT}, CNNM2_{cNMP} and CNNM2_{BAT-cNMP}—The CNNM2_{BAT} protein was produced as described previously (39). Use of EDTA was avoided to preclude Mg^{2+} and Zn^{2+} chelation. Fractions containing the pure protein were concentrated to 20 mg ml⁻¹ and were frozen in liquid nitrogen and stored at -80 °C.

The CNNM2_{cNMP} and CNNM2_{BAT-cNMP} protein constructs were generated by recombinant PCR fusing the cDNA encoding the intracellular cNMP binding domain (amino acid residues 593–875 and STOP) or the C terminus (Bateman domain + cNMP binding domain; amino acid residues 429–875 and STOP) of murine Cnm2 to cDNA encoding a His₆ tag followed by a tobacco etch virus protease cleavage site. The obtained PCR products were cloned into pET22 via BamHI and EcoRI and confirmed by sequencing. Resulting constructs were transformed into *Escherichia coli* BL21 (DE3) and used for protein purification. CNNM2_{cNMP} and CNNM2_{BAT-cNMP} purification involved the use of a nickel affinity column (HisTrap HP, 5 ml, GE Healthcare) to isolate the His₆ tag fused proteins. A

Structure of PRL-1 in Complex with CNNM2

subsequent tobacco etch virus protease cleavage and a second Ni-affinity chromatography step served to eliminate the tag from the protein solution. Finally, a molecular size exclusion chromatographic step using a HiLoad 16/600 Superdex 75 preparation grade in the case of CNNM2_{CNMP} or a HiLoad 16/600 Superdex 200 preparation grade in the case of CNNM2_{BAT-CNMP} (purchased from GE Healthcare) was performed. The isolated pure proteins were aliquoted, flash-frozen in liquid nitrogen, and stored at -80°C .

Expression and Purification of PRLs—Mouse PRL-1 (a kind gift from Qi Zeng, Singapore) that shares 100% amino acid sequence identity with human PRL-1 was amplified by PCR (KAPA HiFi DNA Polymerase, Kappa Biosystem) using specific primers for the Gateway system (Invitrogen) and cloned in pDONR221 according to the manufacturer's instructions. Subsequently, it was shuttled into the bacterial expression vector pDEST17 that contains an N-terminal His₆ tag, according to the Gateway system protocol (Invitrogen). 20-ml starter cultures were grown overnight at 37°C and used to inoculate 2-liter cultures of Luria-Bertani medium containing 100 mg liter^{-1} ampicillin. The cells were grown at 37°C to an $A_{600\text{ nm}}$ of 0.8. Protein expression was induced by the addition of isopropyl β -D-1-thiogalactopyranoside to a final concentration of 1 mM, and the cultures were left shaking for a further 3 h at 37°C . The cells were harvested by centrifugation at $11,000 \times g$ for 20 min at 4°C , resuspended in lysis buffer (50 mM Tris-HCl, pH 8, 300 mM NaCl, 25 mM imidazole, 1 mM DTT, 1 mM benzamidine, 0.1 mM PMSF), and lysed by sonication in a Labsonic P sonicator (Sartorius; 12 cycles of 15 s at 90% amplitude with 60 s resting on ice between each cycle to prevent sample overheating). The cell obtained lysate was clarified by ultracentrifugation at $250,000 \times g$ for 60 min at 4°C , and the supernatant was filtered through a $0.45\text{-}\mu\text{m}$ filter before being applied onto a pre-equilibrated 5-ml HisTrap HP column (GE Healthcare) connected to an AKTA FPLC system (GE Healthcare) installed within a refrigerated cabinet at 4°C . The column was then washed with 10 column volumes of buffer A (50 mM Tris-HCl, pH 8, 300 mM NaCl, 25 mM imidazole, 1 mM DTT), and the bound protein was eluted with buffer B (50 mM Tris-HCl, pH 8, 300 mM NaCl, 300 mM imidazole, 1 mM DTT) using a linear gradient over 30 column volumes. The fractions containing the protein of interest (confirmed by SDS-PAGE) were pooled and concentrated using an Amicon Ultra-15 (5000-Da cutoff) centrifugal concentrator (Millipore) to a volume of ~ 2 ml. Subsequently, the concentrated protein was applied onto a HiLoad Superdex 75 16/60 Prep Grade gel-filtration column (GE Healthcare) pre-equilibrated with 20 mM Tris, pH 8.0, 200 mM NaCl, 1 mM DTT and eluted at a flow rate of 0.3 ml min^{-1} . Fractions containing pure protein were pooled and concentrated to 10 mg ml^{-1} using an Amicon Ultra-4 5000-Da cutoff concentrator (Millipore) and were frozen in liquid nitrogen and stored at -80°C . Human PRL-2 and PRL-3 were obtained following a similar protocol to that used for PRL-1.

Purification of the PRL-1·CNNM2_{BAT} Complex—The pure CNNM2_{BAT} and PRL proteins dissolved in 20 mM Tris, pH 8, 200 mM NaCl, 1 mM DTT were incubated together for periods ranging from 20 min to 12 h at two different temperatures (4 and 20°C). A protein mix containing 2.5 mg of PRL-1 and 1.3

mg of CNNM2_{BAT} in a final volume of 0.5 ml of buffer 20 mM Tris, pH 8.0, 200 mM NaCl, 1 mM DTT (approximate PRL-1/CNNM2_{BAT} molar ratio = 1.5) incubated for 2 h at 4°C of PRL-1, was finally selected as the optimal condition to form the complex. The protein mix was subsequently subjected to size exclusion chromatography analysis (Superdex 200 Increase 10/300 GL column, flow rate of 0.5 ml min^{-1} , 4°C) with buffer consisting of 20 mM Tris, pH 8, 200 mM NaCl, 1 mM DTT. The fractions containing the corresponding PRL·CNNM2_{BAT} complexes (Fig. 1) were pooled and concentrated to $\sim 15\text{ mg ml}^{-1}$ using an Amicon Ultra-15 (5000-Da cutoff) centrifugal concentrator (Millipore) and distributed in aliquots of $25\text{ }\mu\text{l}$ that were subsequently flash-frozen in liquid nitrogen and stored at -80°C . The identity of all independent proteins as well as of those forming the complex was confirmed by mass spectrometry from the corresponding SDS-polyacrylamide gel bands as described previously (39). The approximate molecular mass of PRL-1, -2, and -3 and CNNM2_{BAT} and the PRLs·CNNM2_{BAT} complexes was estimated from a plot representing K_{av} versus $\log M_w$ (where $K_{\text{av}} = (V_e - V_o)/(V_t - V_o)$; V_e = elution volume; V_t = total column volume, and V_o = void volume), using a Superdex 200 Increase 10/300 GL column (GE Healthcare) previously calibrated with commercially available molecular weight standards (Bio-Rad, catalogue no. 151-1901).

Plasmid Construction, Transfection and Pulldown Experiments—Full-length CNNM2 cDNA (a kind gift from J. G. Hoenderop, Radboud Institute for Molecular Life Sciences, The Netherlands) was recombined into pDONR221 entry vector using specific primers and shuttled into pLenti6-v5 destination mammalian expressing vector according to the Gateway system protocols (Invitrogen). Cloning of GST-PRL-1 was previously described (17). Point mutations in CNNM2 were introduced by site-directed mutagenesis using the QuikChange site-directed mutagenesis kit (Stratagene). HeLa cells were cultured in DMEM (HyClone) supplemented with 10% fetal bovine serum (FBS) and $10\text{ }\mu\text{g/ml}^{-1}$ gentamicin at 37°C with 5% CO_2 . Transfections in HeLa cells were performed using Lipofectamine 2000 (Invitrogen) following the manufacturer's instructions, and media were replaced 4 h after transfection. GST pulldowns were carried out 8 or 24 h post-transfection as described previously (17).

Crystallization of the PRL-1·CNNM2_{BAT} Complex—Crystals of the PRL-1·CNNM2_{BAT} complex were obtained in 24 h by the hanging-drop vapor diffusion method at 20°C in 96- and 24-well crystallization plates. Drops consisted of $1\text{ }\mu\text{l}$ of the PRL-1·CNNM2_{BAT} complex solution mixed with $1\text{ }\mu\text{l}$ of precipitant solution (0.1 M sodium acetate, pH 4.6, and 2 M sodium formate). The protein complex concentration was 15 mg ml^{-1} . To obtain the ZnATP-bound complex, the nucleotide (ATP) was independently added to the protein at a final concentration of 3.7 mM, resulting in an $\sim 1:10$ protein-to-nucleotide ratio. ZnCl_2 (used as a source of Zn^{2+} ions) was added at a final concentration of 5 mM. The crystals, obtained under similar conditions (0.1 M sodium acetate, pH 4.6, and 2 M ammonium formate at 20°C) and time (~ 24 h) to those described for the apo-complex, were flash-cooled in liquid nitrogen immediately after they grew. All datasets used in this work were collected at European Synchrotron Radiation Facility (Grenoble, France)

beamlines ID23.1 and ID29 and at ALBA Synchrotron (Barcelona, Spain) beamline MX XALOC-BL13.

X-ray Diffraction Data Collection, Phasing, and Refinement—Diffraction intensities were indexed and integrated by using the software XDS and scaled with XSCALE (48). Data were phased by molecular replacement with PHASER (49) using the structures of the truncated CNNM2_{BAT} construct (residues 429–584, PDB code 4IY0 (37) and PRL-1 (PDB code 1XM2) (13)) as the initial search models. The crystals of apo-PRL-1-CNNM2_{BAT} belong to the *I*222 space group and contain one heterodimer per asymmetric unit. The symmetry operator that generates the biological heterotetramer $2 \times (\text{apo-PRL-1-CNNM2}_{\text{BAT}})$ from the heterodimer is $(-x, -y + 1, z)$. The crystals of the ZnATP-bound PRL-1-CNNM2_{BAT} complex belong to the *C*2 space group and contain one heterotetramer per asymmetric unit. The structures were refined with PHENIX (50) and/or REFMAC5 (51), alternating manual modeling with Coot (52). The actual model does not include residues 579–584 at the C terminus of CNNM2, as well as 23 residues (MSYHHHHHHLEST-SLYKKAGFT) inserted before the N terminus of PRL-1 by the expression vector used. It also lacks the first seven N-terminal residues of PRL-1, and residues 158–173 of the phosphatase. The crystal characteristics and final refinement statistics are summarized in the Table 1. The figures showing three-dimensional protein structures were prepared with PyMOL and Chimera. Calculation of surfaces was done with the PISA server (53).

NMR Analysis—For the ATP hydrolysis experiments, we used the unlabeled CNNM2_{BAT} construct and the PRL-1-CNNM2_{BAT} complex. We then recorded a series of one-dimensional ³¹P NMR spectra (60 ppm spectral width and 3.5 Hz spectral resolution) with inverse gated ¹H decoupling ($B_{\text{rf}} = 2.2$ kHz at 3.5 ppm) on our 600 MHz BRUKER AVANCE III spectrometer equipped with a QXI probe. Its low intrinsic ³¹P detection sensitivity required a 1-h FID accumulation per spectrum for sufficient signal-to-noise ratio, resulting in a 1-h time resolution to monitor ATP hydrolysis. To optimize the signal-to-noise ratio per time, the total interscan recovery delay τ_{total} should be set to $1.25 \times T_1$, with $T_1 =$ longitudinal relaxation time. For the three ³¹P signals of ATP and two ³¹P signals of ADP (1 mM, pH 4.6, 5 mM ZnCl₂), we experimentally derived $T_1 = 340$ – 440 ms, resulting in $\tau_{\text{total}} = 425$ – 550 ms. To level out the slight differences in T_1 and thus allow for quantitative analysis of signal intensities, we increased τ_{total} to $2 \times T_{1, \text{max}} = 880$ ms, resulting in the accumulation of 4096 transients per ³¹P spectrum of 1-h duration. The ³¹P signals of free phosphate, however, has a substantially longer T_1 of 7.4 s. To avoid its increasing saturation, we applied a $\theta \approx 90^\circ$ ³¹P excitation pulse of 285 μ s duration at -15 ppm, at the center of the ATP (and ADP) signals. This medium power pulse achieves only $\theta \approx 20^\circ$ residual excitation for the off-resonant phosphate signal (at 0 ppm), approaching the Ernst angle for optimal signal-to-noise as given by $\cos\theta = \exp(-\tau_{\text{total}}/T_1)$ (54). Thus, saturation of the phosphate ³¹P signal is avoided, however, at the expense of allowing only for semi-quantitative analysis of its intensity.

Isothermal Titration Calorimetry—ITC experiments were performed in an ITC₂₀₀ microcalorimeter (Malvern) in 20 mM Tris, 200 mM NaCl, 1 mM DTT, pH 8, and 25 °C.

Interaction of PRL-1 with CNNM2_{BAT} and CNNM2_{BAT-cNMP}—PRL-1 (540 μ M) was loaded in the titrating syringe and the CNNM2 proteins (CNNM2_{BAT}, 25 μ M; CNNM2_{BAT-cNMP}, at 29 μ M) (or buffer in blank titrations) in the cell. Titrations were performed by stepwise addition of $1 \times 0.5 \mu$ l followed by 18–20 injections of 1.8 μ l, under constant 800 rpm stirring. Heats were integrated, and after subtraction of dilution heats (obtained from titrating buffer with PRL-1), the resulting binding isotherms were analyzed using a single type of independent binding sites model.

Interaction of CNNM2_{cNMP} with PRL-1 and CNNM2_{BAT}—Either CNNM2_{BAT} (23 μ M) or PRL-1 (32 μ M) was placed in the cell and titrated using CNNM2_{cNMP} (0.78 mM) in the syringe in an ITC₂₀₀. Buffer was the same as that used in previous experiments and 25 °C was the experimental temperature. 1×0.5 - μ l + 22×1.5 - μ l injections were performed and spaced at 180 s. A blank titration of CNNM2_{cNMP} (0.78 mM) into buffer was performed using identical conditions. Protein concentrations were determined using the extinction coefficients for the protein monomers (PRL-1, 24,410; PRL-2, 24,410; PRL-3, 25,900; CNNM2_{BAT}, 4470; CNNM2_{cNMP}, 13,410; and CNNM2_{BAT-cNMP} 20,860 M⁻¹ cm⁻¹ at 280 nm, respectively).

PDB Accession Codes—The refined models and structure factors have been deposited in the Protein Data Bank with codes 5MMZ (apo-PRL-1-CNNM2_{BAT}) and 5LXQ (PRL-1-CNNM2_{BAT}·ZnATP).

Author Contributions—D. M., M. L. T., and L. A. M.-C. conceived and coordinated the study and wrote the paper. P. G.-M., I. O., T. B., M. S., and J. E.-O. purified the proteins and performed the crystallographic analysis. S. H. and E. K. cloned and overexpressed the proteins, and performed directed mutagenesis experiments, pulldown, and phosphatase activity assays. A. L. P. performed the ITC analysis. L. A. M.-C., I. O., and T. D. performed the NMR experiments; F. C. M., R. K.-N., and M. L. M.-C. contributed to the design and analyzed the obtained results. All authors reviewed the results and approved the final version of the manuscript.

Acknowledgments—We thank the staff of BL13 (XALOC) beamline at ALBA (Barcelona, Spain) and of ESRF (European Synchrotron Radiation Facility, Grenoble, France) beamlines ID14-1, ID23-1, -2, and ID29, and Diamond (Didcot, UK) beamline I04 for support during synchrotron data collection. We thank Dr. Adriana Rojas for maintenance of the in-house X-ray platform and Nekane Merino for valuable assistance with the size exclusion chromatography experiments.

References

- Zeng, Q., Hong, W., and Tan, Y. H. (1998) Mouse PRL-2 and PRL-3, two potentially prenylated protein-tyrosine phosphatases homologous to PRL-1. *Biochem. Biophys. Res. Commun.* **244**, 421–427
- Zeng, Q., Si, X., Horstmann, H., Xu, Y., Hong, W., and Pallen, C. J. (2000) Prenylation-dependent association of protein-tyrosine phosphatases PRL-1, -2, and -3 with the plasma membrane and the early endosome. *J. Biol. Chem.* **275**, 21444–21452
- Julien, S. G., Dubé, N., Hardy, S., and Tremblay, M. L. (2011) Inside the human cancer tyrosine phosphatome. *Nat. Rev. Cancer* **11**, 35–49

Structure of PRL-1 in Complex with CNNM2

- Hardy, S., Julien, S. G., and Tremblay, M. L. (2012) Impact of oncogenic protein-tyrosine phosphatases in cancer. *Anticancer Agents Med. Chem.* **12**, 4–18
- Diamond, R. H., Cressman, D. E., Laz, T. M., Abrams, C. S., and Taub, R. (1994) PRL-1, a unique nuclear protein-tyrosine phosphatase, affects cell growth. *Mol. Cell. Biol.* **14**, 3752–3762
- Jiao, Y., Ye, D. Z., Li, Z., Teta-Bissett, M., Peng, Y., Taub, R., Greenbaum, L. E., and Kaestner, K. H. (2015) Protein-tyrosine phosphatase of liver regeneration-1 is required for normal timing of cell cycle progression during liver regeneration. *Am. J. Physiol. Gastrointest. Liver Physiol.* **308**, G85–G91
- Sun, J. P., Luo, Y., Yu, X., Wang, W. Q., Zhou, B., Liang, F., and Zhang, Z. Y. (2007) Phosphatase activity, trimerization, and the C-terminal polybasic region are all required for PRL1-mediated cell growth and migration. *J. Biol. Chem.* **282**, 29043–29051
- Zeng, Q., Dong, J. M., Guo, K., Li, J., Tan, H. X., Koh, V., Pallen, C. J., Manser, E., and Hong, W. (2003) PRL-3 and PRL-1 promote cell migration, invasion, and metastasis. *Cancer Res.* **63**, 2716–2722
- Achiwa, H., and Lazo, J. S. (2007) PRL-1 tyrosine phosphatase regulates c-Src levels, adherence, and invasion in human lung cancer cells. *Cancer Res.* **67**, 643–650
- Jin, S., Wang, K., Xu, K., Xu, J., Sun, J., Chu, Z., Lin, D., Koeffler, P. H., Wang, J., and Yin, D. (2014) Oncogenic function and prognostic significance of protein-tyrosine phosphatase PRL-1 in hepatocellular carcinoma. *Oncotarget* **5**, 3685–3696
- Shinmei, S., Sentani, K., Hayashi, T., Sakamoto, N., Goto, K., Zarni Oo, H., Naito, Y., Teishima, J., Matsubara, A., Oue, N., Kuniyasu, H., and Yasui, W. (2014) Identification of PRL1 as a novel diagnostic and therapeutic target for castration-resistant prostate cancer by the *Escherichia coli* ampicillin secretion trap (CAST) method. *Urol. Oncol.* **32**, 769–778
- Lu, J. W., Chang, J. G., Yeh, K. T., Chen, R. M., Tsai, J. J., Su, W. W., and Hu, R. M. (2012) Increased expression of PRL-1 protein correlates with shortened patient survival in human hepatocellular carcinoma. *Clin. Transl. Oncol.* **14**, 287–293
- Jeong, D. G., Kim, S. J., Kim, J. H., Son, J. H., Park, M. R., Lim, S. M., Yoon, T. S., and Ryu, S. E. (2005) Trimeric structure of PRL-1 phosphatase reveals an active enzyme conformation and regulation mechanisms. *J. Mol. Biol.* **345**, 401–413
- Sun, J. P., Wang, W. Q., Yang, H., Liu, S., Liang, F., Fedorov, A. A., Almo, S. C., and Zhang, Z. Y. (2005) Structure and biochemical properties of PRL-1, a phosphatase implicated in cell growth, differentiation, and tumor invasion. *Biochemistry* **44**, 12009–12021
- Yu, L., Kelly, U., Ebricht, J. N., Malek, G., Saloupis, P., Rickman, D. W., McKay, B. S., Arshavsky, V. Y., and Bowes Rickman, C. (2007) Oxidative stress-induced expression and modulation of phosphatase of regenerating liver-1 (PRL-1) in mammalian retina. *Biochim. Biophys. Acta* **1773**, 1473–1482
- Rios, P., Li, X., and Köhn, M. (2013) Molecular mechanisms of the PRL phosphatases. *FEBS J.* **280**, 505–524
- Hardy, S., Uetani, N., Wong, N., Kostantin, E., Labbé, D. P., Bégin, L. R., Mes-Masson, A., Miranda-Saavedra, D., and Tremblay, M. L. (2015) The protein-tyrosine phosphatase PRL-2 interacts with the magnesium transporter CNNM3 to promote oncogenesis. *Oncogene* **34**, 986–995
- Yamazaki, D., Funato, Y., Miura, J., Sato, S., Toyosawa, S., Furutani, K., Kurachi, Y., Omori, Y., Furukawa, T., Tsuda, T., Kuwabata, S., Mizukami, S., Kikuchi, K., and Miki, H. (2013) Basolateral Mg^{2+} extrusion via CNNM4 mediates transcellular Mg^{2+} transport across epithelia: a mouse model. *PLoS Genet.* **9**, e1003983
- de Baaij, J. H., Hoenderop, J. G., and Bindels, R. J. (2015) Magnesium in man: implications for health and disease. *Physiol. Rev.* **95**, 1–46
- Wang, C. Y., Shi, J. D., Yang, P., Kumar, P. G., Li, Q. Z., Run, Q. G., Su, Y. C., Scott, H. S., Kao, K. J., and She, J. X. (2003) Molecular cloning and characterization of a novel gene family of four ancient conserved domain proteins (ACDP). *Gene* **306**, 37–44
- Quamme, G. A. (2010) Molecular identification of ancient and modern mammalian magnesium transporters. *Am. J. Physiol. Cell Physiol.* **298**, Cys-407–Cys-429
- Goytain, A., and Quamme, G. A. (2005) Functional characterization of ACDP2 (ancient conserved domain protein), a divalent metal transporter. *Physiol. Genomics* **22**, 382–389
- Stuiver, M., Lainez, S., Will, C., Terryn, S., Günzel, D., Debaix, H., Sommer, K., Kopplin, K., Thumfart, J., Kampik, N. B., Querfeld, U., Willnow, T. E., Nèmec, V., Wagner, C. A., Hoenderop, J. G., et al. (2011) CNNM2, encoding a basolateral protein required for renal Mg^{2+} handling, is mutated in dominant hypomagnesemia. *Am. J. Hum. Genet.* **88**, 333–343
- Wang, C. Y., Yang, P., Shi, J. D., Purohit, S., Guo, D., An, H., Gu, J. G., Ling, J., Dong, Z., and She, J. X. (2004) Molecular cloning and characterization of the mouse Acdp gene family. *BMC Genomics* **10**, 1186/1471–2164-5–7
- McKusick, V. A. (1998) *Mendelian Inheritance in Man. A Catalog of Human Genes and Genetic Disorders*, 12th Ed., Johns Hopkins University Press, Baltimore, MD
- Lotan, A., Fenckova, M., Bralten, J., Alftoa, A., Dixson, L., Williams, R. W., and van der Voet, M. (2014) Neuroinformatic analyses of common and distinct genetic components associated with major neuropsychiatric disorders. *Front. Neurosci.* **8**, 331
- Arjona, F. J., de Baaij, J. H., Schlingmann, K. P., Lameris, A. L., van Wijk, E., Flik, G., Regele, S., Korenke, G. C., Neophytou, B., Rust, S., Reintjes, N., Konrad, M., Bindels, R. J., and Hoenderop, J. G. (2014) CNNM2 mutations cause impaired brain development and seizures in patients with hypomagnesemia. *PLoS Genet.* **10**, e1004267
- Polok, B., Escher, P., Ambresin, A., Chouery, E., Bolay, S., Meunier, I., Nan, F., Hamel, C., Munier, F. L., Thilo, B., Mégarbané, A., and Schorderet, D. F. (2009) Mutations in CNNM4 cause recessive cone-rod dystrophy with amelogenesis imperfecta. *Am. J. Hum. Genet.* **84**, 259–265
- Parry, D. A., Mighell, A. J., El-Sayed, W., Shore, R. C., Jalili, I. K., Dollfus, H., Bloch-Zupan, A., Carlos, R., Carr, I. M., Downey, L. M., Blain, K. M., Mansfield, D. C., Shahrabi, M., Heidari, M., Aref, P., et al. (2009) Mutations in CNNM4 cause Jalili syndrome, consisting of autosomal-recessive cone-rod dystrophy and amelogenesis imperfecta. *Am. J. Hum. Genet.* **84**, 266–273
- Sponder, G., Mastrototaro, L., Kurth, K., Merolle, L., Zhang, Z., Abdulhanan, N., Smorodchenko, A., Wolf, K., Fleig, A., Penner, R., Iotti, S., Aschenbach, J. R., Vormann, J., and Kolisek, M. (2016) Human CNNM2 is not a Mg^{2+} transporter *per se*. *Pflugers Arch.* **468**, 1223–1240
- Feeney, K. A., Hansen, L. L., Putker, M., Olivares-Yañez, C., Day, J., Eades, L. J., Larrondo, L. F., Hoyle, N. P., O'Neill, J. S., and van Ooijen, G. (2016) Daily magnesium fluxes regulate cellular timekeeping and energy balance. *Nature* **532**, 375–379
- Yamazaki, D., Miyata, H., Funato, Y., Fujihara, Y., Ikawa, M., and Miki, H. (2016) The Mg^{2+} transporter CNNM4 regulates sperm Ca^{2+} homeostasis and is essential for reproduction. *J. Cell Sci.* **129**, 1940–1949
- Bateman, A. (1997) The structure of a domain common to archaeobacteria and the homocystinuria disease protein. *Trends Biochem. Sci.* **22**, 12–13
- Baykov, A. A., Tuominen, H. K., and Lahti, R. (2011) The CBS domain: a protein module with an emerging prominent role in regulation. *ACS Chem. Biol.* **6**, 1156–1163
- Ereño-Orbea, J., Oyenarte, I., and Martínez-Cruz, L. A. (2013) CBS domains: ligand binding sites and conformational variability. *Arch. Biochem. Biophys.* **540**, 70–81
- Shabb, J. B., and Corbin, J. D. (1992) Cyclic nucleotide-binding domains in proteins having diverse functions. *J. Biol. Chem.* **267**, 5723–5726
- Corral-Rodríguez, M. Á., Stuiver, M., Abascal-Palacios, G., Diercks, T., Oyenarte, I., Ereño-Orbea, J., de Opakua, A. L., Blanco, F. J., Encinar, J. A., Spiwok, V., Terashima, H., Accardi, A., Müller, D., and Martínez-Cruz, L. A. (2014) Nucleotide binding triggers a conformational change of the CBS module of the magnesium transporter CNNM2 from a twisted towards a flat structure. *Biochem. J.* **464**, 23–34
- Hirata, Y., Funato, Y., Takano, Y., and Miki, H. (2014) Mg^{2+} -dependent interactions of ATP with the cystathionine- β -synthase (CBS) domains of a magnesium transporter. *J. Biol. Chem.* **289**, 14731–14739
- Gómez-García, I., Stuiver, M., Ereño, J., Oyenarte, I., Corral-Rodríguez, M. A., Müller, D., and Martínez-Cruz, L. A. (2012) Purification, crystallization and preliminary crystallographic analysis of the CBS-domain pair of cyclin M2 (CNNM2). *Acta Crystallogr. Sect. F Struct. Biol. Cryst. Commun.* **68**, 1198–1203

40. Kozlov, G., Cheng, J., Ziomek, E., Banville, D., Gehring, K., and Ekiel, I. (2004) Structural insights into molecular function of the metastasis-associated phosphatase PRL-3. *J. Biol. Chem.* **279**, 11882–11889
41. Kostantin, E., Hardy, S., Valinsky, W. C., Kompatscher, A., de Baaij, J. H., Zolotarov, Y., Landry, M., Uetani, N., Martínez-Cruz, L. A., Hoenderop, J. G., Shrier, A., and Tremblay, M. L. (2016) Inhibition of the PRL-2/CNNM3 protein complex formation decreases breast cancer proliferation and tumor growth. *J. Biol. Chem.* **291**, 10716–10725
42. Bessette, D. C., Qiu, D., and Pallen, C. J. (2008) PRL PTPs: mediators and markers of cancer progression. *Cancer Metastasis Rev.* **27**, 231–252
43. Kleywegt, G. J., and Jones, T. A. (2002) Homo crystallographicus—*quo vadis?* *Structure* **10**, 465–472
44. Denu, J. M., Lohse, D. L., Vijayalakshmi, J., Saper, M. A., and Dixon, J. E. (1996) Visualization of intermediate and transition-state structures in protein-tyrosine phosphatase catalysis. *Proc. Natl. Acad. Sci. U.S.A.* **93**, 2493–2498
45. Bai, Y., Luo, Y., Liu, S., Zhang, L., Shen, K., Dong, Y., Walls, C. D., Quilliam, L. A., Wells, C. D., Cao, Y., and Zhang, Z. Y. (2011) PRL-1 protein promotes ERK1/2 and RhoA protein activation through a non-canonical interaction with the Src homology 3 domain of p115 Rho GTPase-activating protein. *J. Biol. Chem.* **286**, 42316–42324
46. Min, S. H., Kim, D. M., Heo, Y. S., Kim, Y. I., Kim, H. M., Kim, J., Han, Y. M., Kim, I. C., and Yoo, O. J. (2009) New p53 target, phosphatase of regenerating liver 1 (PRL-1) down-regulates p53. *Oncogene* **28**, 545–554
47. Ereño-Orbea, J., Majtan, T., Oyenarte, I., Kraus, J. P., and Martínez-Cruz, L. A. (2013) Structural basis of regulation and oligomerization of human cystathionine β -synthase, the central enzyme of transsulfuration. *Proc. Natl. Acad. Sci. U.S.A.* **110**, E3790–E3799
48. Kabsch, W. (2010) XDS. *Acta Crystallogr. D Biol. Crystallogr.* **66**, 125–132
49. McCoy, A. J., Grosse-Kunstleve, R. W., Adams, P. D., Winn, M. D., Storoni, L. C., and Read, R. J. (2007) Phaser crystallographic software. *J. Appl. Crystallogr.* **40**, 658–674
50. Adams, P. D., Afonine, P. V., Bunkóczi, G., Chen, V. B., Echols, N., Headd, J. J., Hung, L. W., Jain, S., Kapral, G. J., Grosse Kunstleve, R. W., McCoy, A. J., Moriarty, N. W., Oeffner, R. D., Read, R. J., Richardson, D. C., et al. (2011) The Phenix software for automated determination of macromolecular structures. *Methods* **55**, 94–106
51. Murshudov, G. N., Skubák, P., Lebedev, A. A., Pannu, N. S., Steiner, R. A., Nicholls, R. A., Winn, M. D., Long, F., and Vagin, A. A. (2011) REFMAC5 for the refinement of macromolecular crystal structures. *Acta Crystallogr. D Biol. Crystallogr.* **67**, 355–367
52. Emsley, P., Lohkamp, B., Scott, W. G., and Cowtan, K. (2010) Features and development of Coot. *Acta Crystallogr. D Biol. Crystallogr.* **66**, 486–501
53. Krissinel, E., and Henrick, K. (2007) “Protein interfaces, surfaces and assemblies” service PISA at the European Bioinformatics Institute. Inference of macromolecular assemblies from crystalline state. *J. Mol. Biol.* **372**, 774–797
54. Ernst, R. R., and Anderson, W. A. (1966) Application of Fourier transform spectroscopy to magnetic resonance. *Rev. Sci. Instr.* **37**, 93–102